# Supermassive Black Holes in X-rays: From Standard Accretion to Extreme Transients

# Erin Kara<sup>1</sup> and Javier García<sup>2</sup>

<sup>1</sup>MIT; email: ekara@mit.edu

xxxxxx 2025. 00:1–57 Copyright © 2025 by the author(s). All rights reserved

#### **Keywords**

Active Galactic Nuclei (AGN), X-rays, black holes, galaxies

#### **Abstract**

X-rays are a critical wavelength for understanding supermassive black holes (SMBHs). X-rays probe the inner accretion flow, closest to the event horizon, where gas inspirals, releasing energy and driving black hole growth. This region also governs the launching of outflows and jets that regulate galaxy evolution and link SMBH growth to their host galaxies.

This review focuses on X-ray observations of SMBHs, through "standard accretion" in persistent Active Galactic Nuclei (AGN) and in extreme transient events, such as Tidal Disruption Events (TDEs), Changing-Look AGN (CLAGN), and Quasi-Periodic Eruptions (QPEs). We describe the X-ray spectral and variability properties of AGN, and the observational techniques that probe the inner accretion flow. Through understanding the phenomenology and accretion physics in standard, individual AGN, we can better probe more exotic phenomenon, including binary SMBH mergers, or Extreme Mass Ratio Inspirals (EMRIs).

In this review, the reader will discover:

- X-ray variability on timescales from minutes to hours traces accretion near the event horizon.
- X-rays can measure the black hole mass, spin and accretion flow geometry and dynamics.
- In transients like TDEs, X-rays probe the newly formed accretion disk that feeds the black hole.
- QPEs are posited to be EMRIs orbiting accreting SMBHs that would emit low-frequency gravitational waves.
- Future X-ray, time-domain and multi-messenger surveys will revolutionize our understanding of SMBH growth.

<sup>&</sup>lt;sup>2</sup>NASA Goddard Space Flight Center; email: javier.a.garciamartinez@nasa.gov

Contents	
1. INTRODUCTION	2
1.1. A Brief History of Supermassive Black Holes in X-rays	
1.2. A note from the Authors	
2. ACCRETION ONTO COMPACT OBJECTS	4
2.1. The basics of accretion theory	
2.2. Standard Accretion Disk Theory	6
2.3. Relevant Variability Timescales	8
3. KEY X-RAY OBSERVABLES OF STANDARD AGN	11
3.1. Spectral Properties of the X-ray Continuum	11
3.2. Polarization Properties of the X-ray Continuum	
3.3. Variability Properties of the X-ray Continuum	20
3.4. X-ray Reflection Spectroscopy: A Probe of the inner accretion flow and black hole spin	
3.5. Reverberation Mapping: A probe of the disk and corona geometry	28
3.6. The ubiquitous soft excess, and its debated origin	30
3.7. Narrow Emission Iron lines: A Probe of the BLR and Dusty Torus	32
3.8. AGN Outflows: The search for AGN Feedback in action	33
4. EXTREME VARIABILITY IN SUPERMASSIVE BLACK HOLES	35
4.1. Tidal Disruption Events	35
4.2. Changing-Look AGN	38
4.3. Quasi-Periodic Eruptions	40
4.4. Supermassive black hole binary candidates	
5. SUMMARY & OUTLOOK	45

#### 1. INTRODUCTION

# 1.1. A Brief History of Supermassive Black Holes in X-rays

When the astronomical object 3C 273 was first detected (Edge et al. 1959), to most optical telescopes it looked like a star in our Galaxy (and was so-termed a "Quasi Stellar Object" or QSO). But in 1963, astronomers realized that the spectra were highly redshifted, implying a distance of 750 Mpc (z=0.158), and thus the bright 3C 273 was, in fact, the most luminous object ever seen (Hazard et al. 1963, Schmidt 1963). In addition, the optical and radio emission from 3C 273 was variable—on timescales of years, to as short as days (Smith & Hoffleit 1963, Dent 1965), indicating that the size of the emitting region was a few light-days across. In other words, these QSOs were producing more radiation than a trillion stars from a region only the size of our Solar System! Not long-after, theorists inferred that accretion onto supermassive black holes could produce such high luminosities from such compact regions (Salpeter 1964). Gas within the gravitational sphere of influence of the black hole will collide, and thanks to the conservation of angular momentum, will eventually form a rotating accretion disk that emits blackbody radiation at optical/UV wavelengths (Lynden-Bell 1969, Bardeen 1970). Through the combination of spectral and timing observations, the field of supermassive black hole accretion and growth was born.

Concurrent with the discovery of the first QSO (now used interchangeably with the term Quasars), the first X-ray sounding rockets were taking flight (Giacconi et al. 1962). It did not take long to discover that the quasar 3C 273 was also bright in X-rays (Bowyer et al. 1970), and beyond that, X-rays appeared commonplace in all AGN, even in lower

mass, nearby Seyferts (Elvis et al. 1978). Indeed, today, it is widely recognized that X-rays are the most efficient means for unambiguously identifying AGN because: (1) X-rays are ubiquitous in AGN and, (2) X-rays are not subject to "contamination" from starlight, as is often the case at longer wavelengths (Mushotzky et al. 1993).

Repeated measurements led quickly to the discovery that AGN vary much more rapidly in X-rays than they do in optical (Winkler & White 1975, Marshall et al. 1981), sometimes on timescales as short as a few minutes (McHardy et al. 1981). This showed that the X-ray emission region arises deep within the nucleus, probing the very central engine of the AGN. While the  $\sim 10^{4-6}\,\mathrm{K}$  accretion disk could be hot enough to explain the optical emission, the X-rays must come from an even hotter ( $\sim 10^9$  K), and more compact plasma, that we now refer to as the "X-ray corona". This definition is based on the spectral and timing properties observed, while the details of its geometry, location, dynamics, and kinematics are still a matter of research.

Beyond the broadband continuum (well-described in the 2–10 keV band as a powerlaw with photon index  $\Gamma \sim 1.5 - 2$ ), Mushotzky et al. (1978) discovered distinctive features at  $\sim 6.4$  keV due to the fluorescence of iron as electron transitions from the inner-most atomic shell (K-shell in spectroscopic notation). This indicates that the central, hot corona irradiates colder gas that flows around the AGN. This Fe K line is a hallmark of the Xray spectrum and is nearly ubiquitous in local Seyferts (Pounds et al. 1989). Fabian et al. (1989) posited that the fluorescence-emitting gas could be the accretion disk itself, and thus by measuring Doppler and gravitational shifts in the Fe K line, one can estimate properties of the disk, including its inclination, and how far the disk extends towards the black hole (an indicator of the spin; see Section 3.4 for details). And thus by combining X-ray spectral and timing information of AGN, one can measure fundamental properties of the black hole (its mass and spin), and can uniquely probe the regions closest to the event horizon, where most of the accretion power is released. Paraphrasing Prof. Andy Fabian:

"It is quite remarkable that the X-ray corona, which is one of the brightest regions in astronomical objects, is coincidentally located right next to the darkest objects in the Universe, black holes."

# 1.2. A note from the Authors

The last Annual Reviews dedicated specifically to the X-ray spectral and timing properties of AGN was published over thirty years ago (Mushotzky et al. 1993), before the launch of our two X-ray flagship missions, Chandra and XMM-Newton, and before even the launch of the first X-ray CCDs on the ASCA mission. The past decade has seen a true revolution in our understanding of the inner accretion flows of AGN, thanks, in large part, to these two flagships and a suite of small, dedicated X-ray telescopes each opening a new and unique parameter space (e.g.; Swift, NuSTAR, AstroSAT, NICER, Insight-HXMT, IXPE, and XRISM).

Beyond advancements specific to the X-ray band, the field of black hole accretion is seeing a renaissance in the wider astronomical community in the last 5-10 years, thanks to the advent of wide-field, time-domain surveys across the electromagnetic spectrum. These surveys monitor hundreds of thousands of AGN at unprecedented cadence, revealing the secrets AGN were keeping while we weren't watching. Time domain surveys are changing what we thought we understood about standard AGN activity, and thus, evolving our

# X-ray Corona: Billion degree

optically-thin plasma where the X-ray continuum originates.

#### CCD:

Charge-CoupledDevice; a commonly used detector that converts light into electronic impulses.

picture of how supermassive black holes grow and affect their environments.

In writing this Annual Review, we aim to describe what we know about "Standard AGN", and how we can use X-ray and multi-wavelength properties to understand their mass, spin, and accretion flow properties (Chapters 2 and 3). It is only if we truly understand "Standard AGN" that we will be able to make sense of the new exotic transients being discovered through time-domain and multi-messenger surveys (Chapter 4).

In a short review, it is impossible to cover all of AGN in X-rays. Admittedly, we limit the present discussion to our areas of expertise, in the X-ray spectral and timing observations of luminous ( $L > 0.01~L_{\rm Edd}$ ), low-obscuration ( $N_H < 10^{23}~{\rm cm}^{-2}$ ), largely radio-quiet ( $L_{1400~{\rm MHz}} < 30~\mu{\rm Jy}$ ), local (z < 1) AGN. In other words, we focus this review on observations of the central engines of supermassive black holes (SMBHs) at the time in their evolution of rapid growth. For readers interested in these other topics, we refer to other recent Annual Reviews: for simulations, see Davis & Tchekhovskoy (2020); for AGN jets, see Blandford et al. (2019); for AGN outflows, see King & Pounds (2015); for obscured AGN, see Hickox & Alexander (2018a), for low-luminosity AGN, see Yuan & Narayan (2014); for AGN feedback, see Fabian et al. (2012).

MHD: Magneto-Hydro-Dynamics; the time-dependent solution of fluid equations in magnetic fields. We aim for this review to not only be a tool for X-ray astronomers, but also for the broader community working on time-domain and multi-messenger astrophysics, MHD simulations of black holes, and high-z quasars with JWST, who would like to understand better what to expect from X-ray observations of standard AGN, and how extreme accretion deviates from our standard picture. We hope this review will build connections across several sub-fields of black hole accretion by highlighting what we have collectively learned in recent years, thus facilitating future discoveries.

#### 2. ACCRETION ONTO COMPACT OBJECTS

The high-energy X-rays observed from AGN are not directly emitted by the accretion disk, but the radiation is primarily powered by accretion processes onto the black hole, which we review here (for details on the X-ray emitting region, see Sec. 3.1.2). This Section begins with an overview of accretion theory, used to describe flows influenced by the gravitational potential of black holes, neutron stars, and, to some extent, white dwarfs. Readers seeking a more detailed discussion are encouraged to consult works such as Armitage (2022), Abramowicz & Fragile (2013), and Davis & Tchekhovskoy (2020).

While the fundamentals of accretion theory discussed here are simplified, they form the basis of much of the historical interpretation of AGN observations. Over the past decade, advancements in computing and simulations have enabled more realistic models of black hole accretion flows, that include 3D effects and radiation. These theoretical developments allows us to start making comparison to observations, and present both opportunities and challenges for theorists to refine models that match the requirements of increasingly sophisticated observational data.

#### 2.1. The basics of accretion theory

The two most fundamental quantities to describe an accretion disk around a black hole are the mass M and the rate at which mass from the accretion disk falls into the black hole,  $\dot{M}$ . The total mass determines the size scale of the system through the *Schwarzschild radius*,

which coincides with the radius of the event horizon in a non-spinning black hole:

$$R_s = 2R_g = \frac{2GM}{c^2} \simeq 3\left(\frac{M}{M_{\odot}}\right) \text{km}$$
 1.

where  $R_g$  is the gravitational radius, G is the Newtonian gravitational constant and c is the speed of light. To give a sense of how compact black holes can be, a  $10^8$  solar masses black hole has a horizon of  $R_s \sim 1$  AU, fitting comfortably within the Earth's orbit.

The extraction of gravitational potential energy through accretion is likely the most efficient and powerful mechanism for the production of high-energy radiation. This can be shown by simple order-of-magnitude estimates. For a body of mass M and radius R, the gravitational potential energy released by accretion of a particle of mass m onto its surface is

$$\Delta E_{acc} = \frac{GMm}{R},$$

In the interior of stars, the burning of hydrogen through nuclear fusion releases no more than 1% of the rest-mass energy,  $\Delta E_{nuc} = 0.01mc^2$ . Dividing these two one gets

$$\frac{\Delta E_{acc}}{\Delta E_{nuc}} = 10^2 \left(\frac{R_g}{R}\right).$$
 3.

Thus, for a Schwarzschild black hole  $(R=2R_g)$ , the energy released from accetion is  $\sim 50$  times that released from nuclear burning. More detailed estimates predict that up to 40% of the rest mass of the accreted material can be emitted as radiation (McClintock & Remillard 2006).

The accretion rate defines the total luminosity of the system

$$L = \eta \dot{M}c^2 \tag{4}$$

Here  $\eta$  is the efficiency of converting the rest-mass energy of the infalling material into radiation. Importantly, whatever is not converted into luminosity  $((1 - \eta)Mc^2)$  is accreted onto the black hole, increasing its mass.

There exist a critical accretion rate at which the outward radiation pressure stops the inward accretion of material. This situation is known as the  $Eddington\ limit$ . Assuming spherical accretion of hydrogen gas onto a compact object of mass M, if the gravitational attraction at a radius r is balanced with the radiation pressure:

$$\frac{GMm_p}{R^2} = \frac{L\sigma_T}{4\pi R^2 c}$$
 5.

where  $m_p$  is the mass of the proton (much larger than the electron mass), and  $\sigma_T = 8\pi e^4/3m_e^2c^4 \approx 6.64 \times 10^{-25} \,\mathrm{cm}^2$  is the Thomson cross section for electron scattering, then the Eddington Luminosity is

$$L_{Edd} = \frac{4\pi G M m_p c}{\sigma_T} \simeq 1.26 \times 10^{44} \left(\frac{M}{10^6 M_{\odot}}\right) \text{erg s}^{-1}.$$
 6.

Although the assumption of spherical symmetry is likely an oversimplification, observational evidence suggest that most accreting systems appear to largely obey it. The Eddington luminosity also implies a critical accretion rate given by

$$\dot{M}_{Edd} = \frac{L_{Edd}}{\eta c^2} \simeq 0.03 \left(\frac{M}{10^6 M_{\odot}}\right) \left(\frac{0.08}{\eta}\right) M_{\odot} \text{ yr}^{-1}.$$

R<sub>ISCO</sub>: Radius of the inner-most circular orbit; is the smallest radius at which a test particle can sustain stable circular orbits around a black hole (or neutron star).

The efficiency of accretion can be estimated by comparing the binding energy of a particle at the innermost stable circular orbit (ISCO) with its rest mass energy  $E = mc^2$ .

For a non-spinning black hole  $R_{\rm ISCO} = 6R_g$  (Kaplan 1949), and using the Newtonian expression for the binding energy

$$E_b = \frac{GMm}{2R_q} = \frac{mc^2}{12}$$
 8.

then

$$\eta = \frac{1}{12} = 0.08 \tag{9}$$

A more detailed calculation taking into account the space-time curvature close to the black hole reduces the binding energy to  $\eta = 0.057$  (Salpeter 1964).

# 2.2. Standard Accretion Disk Theory

The most standard semi-analytical treatment of the theory of accretion disks is that by Shakura & Sunyaev (1973) and Novikov & Thorne (1973), the latter including a fully relativistic framework. Here we simply mention some of the most important derivations, and for simplicity we will follow the classical approach of Shakura & Sunyaev (1973) (hereafter, SS73).

The standard theory considers a geometrically thin accretion disk (i.e.  $H \ll R$ , where H is the scale height at radius R), such that the gas particles follow Keplerian orbits at each radius and the inward radial speed is much smaller than the rotation velocity. The internal viscosity of the gas produces a loss of energy and angular momentum of the particles. This model prescribes that the viscosity  $\nu$  in the gas is given by

$$\nu = \alpha c_s H, \tag{10.}$$

where  $c_s$  is the sound speed and  $\alpha$  is the dimensionless parameter between 0 and 1, describing the efficiency of angular momentum transport. Recent numerical simulations of accretion disks suggest that  $\alpha \sim 0.01-0.1$  (e.g.; Hawley et al. 1995, Stone et al. 1996). With the SS73  $\alpha$ -disk model that many works still follow, we have parametrized our ignorance on the physical mechanisms responsible for the transport of angular momentum outward, which is required to enable accretion of material inward. The excess of energy will be used to heat the gas and is ultimately radiated away. The emerging flux at each radius, assuming the same accretion rate over the disk, is given by

$$F_d(R) = \frac{3GM\dot{M}}{8\pi R^3} \left[ 1 - \left(\frac{3R_s}{R}\right)^{1/2} \right].$$
 11.

From here, the effective temperature can easily be derived through the Stefan-Boltzmann relation  $F = \sigma T_{eff}^4$  ( $\sigma \simeq 5.67 \times 10^{-5}\,\mathrm{erg\,cm^{-2}\,s^{-1}\,K^{-4}}$ ). Therefore, we see that  $R,\,M$  and  $\dot{M}$  determine the structure of the disk in the standard model. Also, SS73 found that for fixed values of M and  $\dot{M}$ , the disk can be divided into three regions depending on R, that determine the gas density profile: the *outer region* at a large R, in which gas pressure dominates radiation pressure and the opacity is controlled by free-free absorption; the *middle region* at smaller R, in which gas pressure is dominated by radiation pressure but the opacity is mainly due to electron scattering; and the *inner region* at very small R, where radiation pressure dominates over the gas pressure, but still scattering dominates the

absorption opacity. For some values of the accretion rate, the middle region may not exist. For a  $10^6 M_{\odot}$  black hole accreting at 1% of the Eddington limit, and assuming  $\alpha = 0.1$  the boundary between the inner and middle regions is at  $R_{im} \sim 40 R_g$ , and between the middle and outer regions at  $R_{mo} \sim 700 R_g$ .

Since the focus of this review is on the X-ray band, where emission originates at the smallest scales, we summarize here the important equations of SS73 for the radiation-dominated case (inner region):

Half-thickness

$$z[\text{cm}] = 3.2 \times 10^6 m\dot{m} \left(1 - r^{-1/2}\right)$$
 12.

Surface density

$$u[\text{gr cm}^{-2}] = 4.6\alpha^{-1}\dot{m}^{-1}r^{3/2}\left(1 - r^{-1/2}\right)$$
 13.

Midplane temperature

$$T[K] = 2.3 \times 10^7 (\alpha m)^{-1/4} r^{-3/8}$$
 14.

Optical depth<sup>1</sup>

$$\tau = 8.2 \times 10^{-5} \alpha^{-17/16} m^{-1/16} \dot{m}^{-2} r^{57/16} \left( 1 - r^{-1/2} \right)^{-2}$$
 15.

Here we used the dimensionless parameter definitions

$$m \equiv \frac{M}{M_{\odot}}$$
  $\dot{m} \equiv \frac{\dot{M}}{\dot{M}_{Edd}}$   $r \equiv \frac{R}{3R_s}$  16.

Then we can also calculate the scale height H = z/r, and the density as

$$n[\text{cm}^{-3}] = \frac{u}{2m_n z}.$$
 17.

So we also have an estimate of the pressure of the gas.

The SS73  $\alpha$ -disk model has been the foundation of subsequent research on accretion disk theory, as it provides a very simple approximation to the global disk properties. However, this prescription does not adequately explain many observational aspects of AGN, such as their UV luminosity and variability (e.g. Alloin et al. 1986 and see Section 3.3). Furthermore, the SS73 model is both thermally and viscously unstable, and thus it cannot be a correct solution for the inner regions of the accretion disk<sup>2</sup>. Theoretical work and numerical simulations have identified MRI—to be the leading process for turbulence in the accretion disk and thus as a main source of pseudo-viscosity (Balbus & Hawley 1991), suggesting that accretion disks are not the idealized steady-state equilibrium assumed by the SS73 model. Thus, the inner regions of luminous disks in AGN (particularly the radiation-pressure-dominated regions) are still poorly understood theoretically, and it is possible that the interpretation of future observational data may lead to changes in current paradigms.

# MRI:

Magneto-rotational instability; fundamental property of ionized accretion flows that generates turbulence, acting as effective viscosity to transport angular momentum outward.

<sup>&</sup>lt;sup>1</sup>Note that this expression differs from the one appearing in SS73, in the radial dependency. In SS73 it appears as  $\propto r^{-93/32}$ , which is likely incorrect, as it would imply an optically-thin disk. Equation 15 was derived using Eqs. 13, 14 and 17 into  $\tau = \sqrt{\sigma_T \sigma_{ff}} u_0$ , with  $\sigma_T = 0.4$  and  $\sigma_{CC} = 0.11 T^{-7/2} n$ , both in cm<sup>2</sup>/gr

 $<sup>\</sup>sigma_{ff}=0.11T^{-7/2}n$ , both in cm²/gr. <sup>2</sup>Models that do not have these instabilities include magnetically supported models (e.g., Begelman & Pringle 2007), which in general have rather different physical conditions as a result.

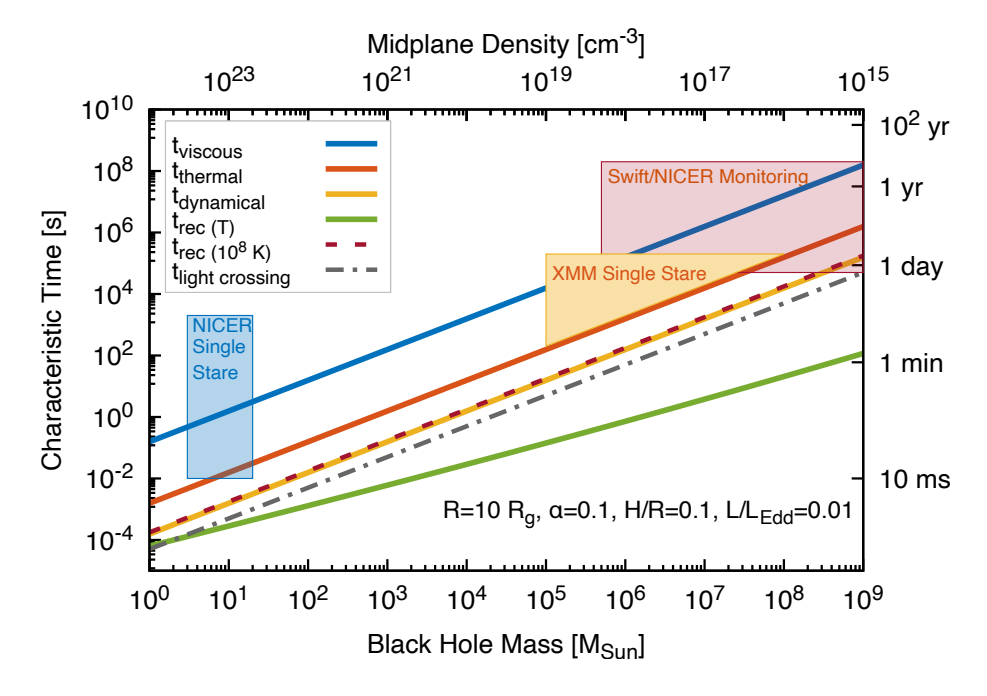


Figure 1

Characteristic timescales relevant for an accretion flow in the innermost regions as a function of the black hole mass. The recombination time  $t_{\rm rec}(T)$  is shown assuming the disk mid-plane density (Eq. 14), as well as the typical temperature ( $T=10^8$  K) of an X-ray irradiated disk surface. The shaded boxes indicate the timescales probed in typical XMM-Newton, Swift and NICER campaigns. (Note that NuSTAR and XRISM are capable long stares that probe timescales similar to XMM-Newton for AGN, but because they both are in Low-Earth Orbit, they have orbital gaps every  $\sim$  90 minutes that make traditional Fourier timing analyses more cumbersome, e.g., Lewin et al. 2022.)

# 2.3. Relevant Variability Timescales

Accretion of matter onto a black hole is an inherently turbulent phenomena, which yields strong variability at many different time scales. It is thus relevant to review the characteristic times, as they provide reasonable estimates for the observed variability.

Perhaps the most fundamental timescale is the light crossing time for photons to travel from the corona to the disk, and from the disk to the observer. In flat space-time (i.e., without relativistic corrections), the light-crossing time is simply  $t_{\rm lc} = R/c$ , where R is the mean distance traveled by the observed photons. This is the timescale responsible for the reverberation time delays observed from IR to X-rays, due to the irradiation of different gas flows around the central engine (Section 3.5.1).

The other different timescales related to variability in AGN can be divided into two main groups; those produced by *accretion processes*, which will then characterize the properties of the infalling material and its overall structure; and those produced by *microscopic processes*, which are connected with the local properties of the plasma (e.g., thermodynamics and ionization state), and with its composition (elemental abundances and atomic properties).

For the accretion flow, the most relevant timescales are:

### • Dynamical time:

$$t_{\rm dyn} \sim \frac{1}{\Omega} = \frac{t_{\rm orb}}{2\pi},$$
 18.

where  $\Omega$  is the angular frequency  $\Omega = (GM/R^3)^{1/2}$ , and  $t_{\rm orb}$  is the orbital time (i.e., the time it takes a particle at a distance R to complete one revolution around the black hole). The angular frequency is sometimes interpreted as the cause of rare quasi-periodic signals seen in a few AGN and TDEs (Gierliński et al. 2008, Pasham et al. 2019, Masterson et al. 2025 and see Section 4.3).

## • Hydrostatic time:

$$t_{\rm hydro} \sim \frac{H}{c_{\rm s}},$$
 19.

is the characteristic time under which the different pressures (e.g.; gas, radiation, gravity) present in the system cancel out such that hydrostatic equilibrium is achieved. This time is mainly controlled by the sound speed in the medium, as no mechanical changes to density or pressure can propagate faster than  $c_s$ . Using the fact the disk scale height is  $H = c_s/\Omega$ , then

$$t_{\rm hydro} \sim \frac{1}{\Omega} = t_{\rm dyn}.$$
 20.

#### • Thermal Time:

$$t_{\rm th} \sim \frac{1}{\alpha \Omega} = \frac{1}{\alpha} t_{\rm dyn},$$
 21.

is the timescale under which a disk annulus will cool down by releasing all its thermal energy if the heating mechanisms are instantaneously suppressed. It also indicates the shortest time under which the disk emission is expected to change as a result of variations in heating by viscosity.

#### • Viscous time:

$$t_{\rm visc} \sim \frac{R^2}{\nu},$$
 22.

sometimes also referred to as the radial infall timescale, it is the time over which the viscosity  $\nu$  in the flow will flatten any gradients in the surface density (Armitage 2022). Invoking the SS73 viscosity prescription (10):

$$t_{\rm visc} \sim \frac{1}{\alpha \Omega} \left(\frac{H}{R}\right)^{-2} = \frac{1}{\alpha} \left(\frac{H}{R}\right)^{-2} t_{\rm dyn},$$
 23.

which in other words, is the characteristic time under which viscosity leads to transport of angular momentum outward allowing for material inflow. A more extensive discussion on these timescales can be found in reviews dedicated to the physics of accretion flows, such as Frank et al. (2002) and Armitage (2022).

In terms of microscopic processes, there are timescales concerning the interaction of radiation and matter. In the context of accretion disks in AGN, where there is strong irradiation of X-rays from the hot corona, these are mostly related to the microscopic properties of the gas. In general, there is a long list of atomic processes that can occur

# **Summary of Characteristic Time Scales**

The relevant timescales in the innermost regions close to the black hole can be summarized as follows:

# **Light Crossing Time**

$$t_{\rm lc} = R/c \sim 50 \,[{\rm s}] \left(\frac{M}{10^6 M_{\odot}}\right) \left(\frac{R}{10 R_g}\right)$$

#### **Accretion Flow**

$$t_{\rm dyn} = \frac{1}{\Omega} \sim 3 \left[ \min \right] \left( \frac{M}{10^6 M_{\odot}} \right) \left( \frac{R}{10 R_g} \right)^{3/2}$$
 25.

$$t_{\rm th} = \frac{1}{\alpha\Omega} \sim 27 \,[{\rm min}] \left(\frac{0.1}{\alpha}\right) \left(\frac{M}{10^6 M_{\odot}}\right) \left(\frac{R}{10 R_q}\right)^{3/2}$$
 26.

$$t_{\rm visc} = \frac{1}{\alpha} \left(\frac{H}{R}\right)^{-2} \frac{1}{\Omega} \sim 44 \,[\text{hours}] \left(\frac{0.1}{\alpha}\right) \left(\frac{0.1}{H/R}\right)^2 \left(\frac{M}{10^6 M_{\odot}}\right) \left(\frac{R}{10 R_g}\right)^{3/2}$$
 27.

# **Microphysics**

$$t_{\rm PI} \sim 3.1 \times 10^{-6} \,[{\rm ms}] \left(\frac{0.1}{\kappa_{\rm x}}\right) \left(\frac{0.1}{\lambda_{\rm Edd}}\right) \left(\frac{M}{10^6 M_{\odot}}\right) \left(\frac{R}{10 R_g}\right)^2$$
 28.

$$t_{\rm rec} \sim 7 \,[{\rm min}] \left(\frac{n}{10^{15}}\right)^{-1} \left(\frac{T}{10^8}\right)^{1.7}$$
 29.

at very different timescales, and can also differ substantially among ions with different nuclear and electric charges. The two most important timescale are the *photoionization* and *recombination* times, which are discussed more extensively in the Appendix. All these timescales are summarized in the Sidebar entitled *Summary of Characteristic Time Scale*.

The characteristic timescales discussed above are shown as a function of the black hole mass in Figure 1, compared to the duration of typical X-ray observing campaigns. The curves are computed for typical parameters in the innermost regions of bright AGN; e.g., inner radius  $(10R_g)$ , alpha parameter  $(\alpha=0.1)$ , aspect ratio (H/R=0.1), and luminosity  $(L=1\%L_{\rm Edd})$ . The density is assumed to be that of the disk mid-plane in a SS73 model. In such a case, the recombination time is much shorter than any of the other relevant times, with the exception of the photoionization time, which is much shorter by several others of magnitude, and thus not shown in the figure (for simplicity, we have followed the approach of García et al. (2013), assuming a pure hydrogen and constant density medium).

However, the recombination time is also a strong function of the gas temperature. In the case of a disk illuminated by the strong radiation from the X-ray corona, the temperature at the surface can reach much higher values, even close to the Compton temperature ( $T \sim 10^7 - 10^9$  K, independently of the black hole mass), as predicted by ionized reflection calculations (e.g.; García & Kallman 2010, García et al. 2013). This hot layer can still

# Compton Temperature:

 $T_{\rm C} = \langle E \rangle /4k$ , temperature where photons undergoing repeated electron scatterings reach balance in energy lost and gained ( $\langle E \rangle$  is mean photon energy).

have a considerable optical depth (e.g.;  $\tau \sim 1-3$ ), depending on the strength of the incident flux. At such high temperatures, the recombination times become much longer, even at the relatively high density predicted for the disk mid-plane. For example, for a temperature of  $T=10^8\,\mathrm{K}$ , the recombination time coincidentally becomes almost identical to the dynamical time scale across all masses, at a radius of  $10\,R_g$ . This situation is exacerbated if the surface density is lower than at the mid-plane, which is more plausible than the density being constant throughout the disk's vertical extension.

Other important times related to the microphysics of the accretion flow, such as the thermal equilibrium time and the photon propagation time are discussed elsewhere (e.g.; García et al. 2013, Rogantini et al. 2022, Sadaula et al. 2023). These recent works represent the initial steps of a complex problem of time-dependent photoionization coupled with the macroscopic properties of the accreted material. Their results clearly indicate the need to expand these studies, to properly account for all the physics relevant to accreting systems.

# 3. KEY X-RAY OBSERVABLES OF STANDARD AGN

The process of growing a black hole through the accretion of matter releases an extraordinary amount of energy (Eq. 4). For luminous AGN of  $10^6-10^8~M_{\odot}$ , most of that emission is released in the EUV and in X-rays from very close to the black hole (within  $\sim 10R_g$ ). With the EUV obscured by Galactic photoelectric absorption, X-rays offer a powerful means to study these energetic environments. Thus, X-rays directly probe how black holes grow via accretion and how AGN are powered.

Figure 2 schematically summarizes the topics in this Section. The primary emission of an AGN is seen from the disk (Sec. 3.1.1) and corona (Sec. 3.1.2). The emission from the corona is polarized (Sec. 3.2), highly variable (Sec. 3.3), and in addition to shining the observer, it also shines back on the accretion disk, causing reprocessed emission, often referred to as "reflection" (Sec. 3.4). We see this reflected light in both X-ray fluorescence lines and in the UV/optical, and it is delayed with respect to the coronal continuum because of the additional light-travel path it has taken (Sec. 3.5.1). The corona also shines light on more distant gas flows around the black hole, from the broad line region and dusty torus (Sec. 3.7) to outflows that may be responsible for AGN feedback (Sec. 3.8). Throughout this section, we often compare the results of AGN to black hole X-ray binaries (see Sidebar entitled Stellar-Mass Black Holes).

# 3.1. Spectral Properties of the X-ray Continuum

3.1.1. The accretion disk and its relationship to the X-ray corona. Fundamentally, as matter funnels towards the black hole through the accretion disk, angular momentum is lost via viscous processes, heating up the disk, and producing multi-temperature thermal emission. This emission is seen directly in the optical/UV and often referred to in undergraduate astrophysics textbooks as "the big blue bump". For luminous black holes of  $10^6 - 10^8 \ M_{\odot}$ , most of the power output from the thermal disk peaks in the EUV, in the unobservable gap imposed by Galactic photoelectric absorption. This complicates studies attempting to calculate the bolometric luminosity,  $L_{\rm Bol}$ , though there have been several attempts to bridge that gap, either by developing physical models for the accretion flow (e.g.; Marconi et al. 2004, Done et al. 2012a), or by assuming agnostic phenomenological models (e.g.; Grupe

Bolometric luminosity,  $L_{\rm Bol}$ : Total intrinsic power released from the accretion process across all wavelengths.

#### STELLAR-MASS BLACK HOLES

Stellar-mass black holes with stellar companions are intriguing and convenient systems to test our theories of accretion. Whereas AGN fueling from the host galaxy is notoriously complex, in black hole X-ray binaries (BH XRBs) with low-mass companions, the feeding is well understood to be from the companion star filling its Roche lobe. As such, one observes an accretion disk, corona and jets, but no torus or broad line region. Whereas AGN emit across the entire electromagnetic spectrum, in BH XRBs, the accretion disks are hotter, and so both the disk and corona emit in X-rays. This allows us to track the disk-corona connection with a single X-ray instrument. Finally, the variability scales with the mass of the black hole (Fig. 1). In BH XRBs the typical light travel time of reverberation out to  $10~R_g$  is  $\sim 0.1$  ms, and therefore, even in a typical NICER observation of just a few kiloseconds in duration, we can measure (with better signal-to-noise) the kinds of time lags it would take days to even years to measure in AGN.

The scaling between AGN and stellar-mass black holes is demonstrated in Fig. 7, where we show an example of the low- and high-frequency X-ray lags for a bright variable AGN Ark 564 ( $M_{\rm BH} \sim 10^6 M_{\odot}$ ) compared to the black hole low-mass X-ray binary MAXI J1820+070 ( $M_{\rm BH} \sim 10 M_{\odot}$ ) taken during the luminous hard state, when  $L/L_{Edd} \sim 0.1$ . They look remarkably similar, but the amplitude of the lag is  $10^5$  times shorter for the stellar-mass black hole. (see Sec. 3.5.1 for more details on reverberation).

This scaling with mass affords the opportunity to measure reverberation lags at different stages of accretion in BH XRBs. While the typical duty cycle of an AGN is expected to be  $\sim 10^{6-8}$  years, the equivalent in an X-ray binary is  $\sim 1$  year. Indeed, the typical duration of an outburst from and X-ray binary is several months. By measuring X-ray reverberation lags at several epochs, we can quantify how the corona, disk and jet evolve together over time (De Marco et al. 2017, Kara et al. 2019, Wang et al. 2021).

et al. 2010). As such, caution is warranted in reading estimates of bolometric luminosity, and even more so the Eddington ratio,  $\lambda_{\rm Edd} \equiv L_{\rm Bol}/L_{\rm Edd}$ , used as a proxy for the mass accretion rate, because that also folds in uncertainties in our measurements of the black hole mass.

The accretion process also leads to strong X-ray emission, as thermal disk photons (so-called "seed" photons) interact with hot ( $\sim 10^9 \, \mathrm{K}$ ) electrons in the central corona, and are inverse Compton upscattered to X-ray energies (Sec. 3.1.2). Several studies have attempted to calculate the ratio of X-ray to bolometric luminosity: Some focus on small samples in the nearby Seyferts (Vasudevan & Fabian 2007, Jin et al. 2012, Duras et al. 2020), in which the broadband SED can be measured and modeled with care (also accounting for the fact that AGN vary and thus optical and X-ray measurements should be made simultaneously). Others have corroborated these studies with large surveys, such as COSMOS (Lusso et al. 2010) and eROSITA eFEDS (Liu et al. 2022), where the sheer number of AGN precludes careful studies of any one, but improves statistics. From these varied approaches, there is general agreement that about 1-20% of the bolometric luminosity is radiated in X-rays, though this value depends strongly on luminosity and mass accretion rate: The ratio of X-ray-to-bolometric luminosity<sup>3</sup> decreases from  $\sim 10\%$  in AGN with  $L_{\rm Bol} \sim 4 \times 10^{42-44}$  erg/cm<sup>2</sup>/s,

<sup>&</sup>lt;sup>3</sup>There have been many studies working to quantify how much energy is released in the accretion disk vs. the corona. Often one sees this parametrized as  $\alpha_{ox}$  (Tananbaum et al. 1979), which is the power-law slope between the 2500 Å luminosity and the 2 keV luminosity. This parametrization

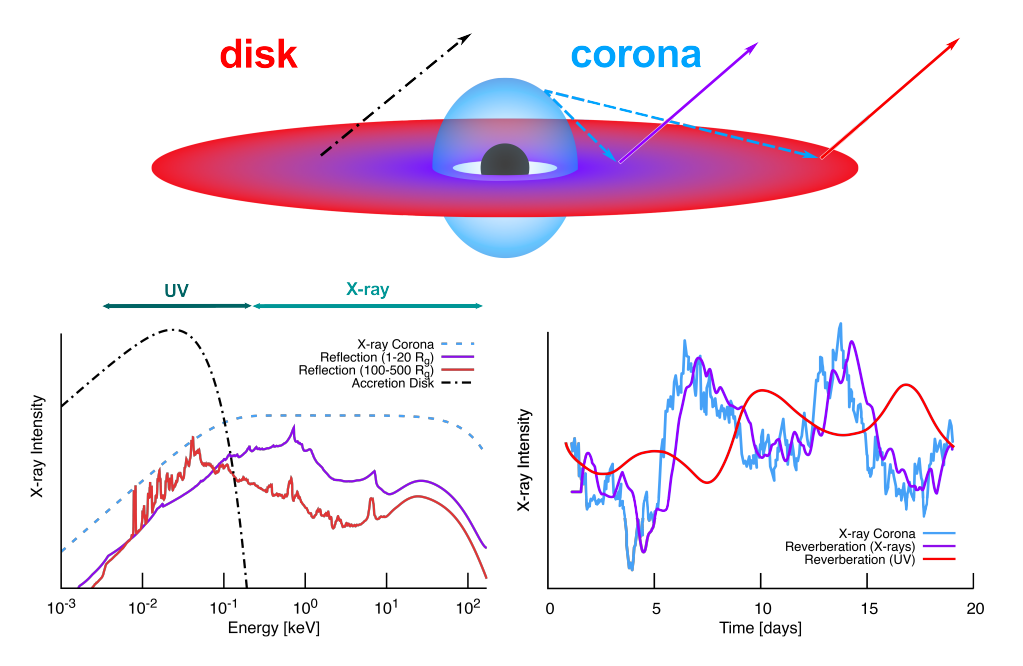


Figure 2

Schematic view of the inner regions of an AGN (top), together with the corresponding UV-to-X-ray spectra and light curves. Bottom-left: The AGN continuum consists of thermal blackbody emission from the disk (black) and X-rays from the corona (blue). The corona will inevitably irradiate the disk, causing the reflection spectra, where the inner-disk reflection dominates in X-rays (purple) and outer-disk reflection peaks in the UV (red). Bottom-right: The reflection spectra are delayed with respect to the continuum (a process known as "reverberation"). X-ray reverberation time delays in purple are short ( $\sim$  minutes for a  $10^7 M_{\odot}$  black hole, or tens of  $R_g$ ), while UV reverberation time delays in red are longer ( $\sim$ days for a  $10^7 M_{\odot}$  black hole, or hundreds of  $R_g$ ). Figure schematics courtesy of Joanna Piotrowska (Caltech). X-ray light curve schematic courtesy of Guglielmo Mastroserio (INAF).

down to  $\sim 1\%$  in AGN with higher luminosities,  $L_{\rm Bol} \sim 4 \times 10^{46}~{\rm erg/cm^2/s}$ . Moreover, there is a noted dependence on mass accretion rate, where the *X-ray-to-bolometric luminosity decreases with increasing M*: from  $\sim 10\%$  at  $\lambda_{\rm Edd} \sim 0.01$  down to 2% at  $\lambda_{\rm Edd} \sim 1$ . Interestingly, these numbers so far do not appear to evolve with redshift, at least up to z=3.5 (though note the interesting new results on high-redshift "Little Red Dots" with *JWST* that, if truly all AGN, appear to be very X-ray weak; Yue et al. 2024, Maiolino et al. 2024).

has the benefit of being model independent, and easy to measure. A smaller  $\alpha_{\rm ox}$  generally means a lower ratio of X-ray-to-bolometric luminosity. The corona-to-disk power is also often quantified as a bolometric correction or 'K-correction', where  $\kappa_{\rm x} = L_{\rm Bol}/L_{\rm x}$ . There is a general correlation between  $\alpha_{\rm ox}$  and  $\kappa_{\rm x}$ . While model-dependent, we choose to quote the ratio of X-ray to bolometric luminosity  $(L_{\rm x}/L_{\rm Bol})$  because we find it most intuitive.

# Origin of the Power-law Continuum

#### **Inverse Compton Scattering**

The "standard" Compton scattering process considers the collision of an energetic photon with an electron at rest. The photon transfers some of its initial energy  $E_i$  to the electron's kinetic energy, emerging after the interaction with a final energy  $E_f$  given by the well known Compton formula:

$$E_f = \frac{E_i}{1 + E_i/m_e c^2 (1 - \cos \theta)},$$
 30.

where  $\theta$  is the angle between the photon's initial and final trajectory. However, if the electron has a kinetic energy comparable to the energy of the photon, then energy can be transfer in the opposite way—from the electron to the photon—a process known as inverse Compton scattering, which can be particularly important for a gas with relativistic electrons. Considering the initial and final energies and scattering angles in both the laboratory and electron's rest frames, an equivalent Compton formula for the energy shift can be written, but its derivation is much too long for this review (details can be found in specialized literature such as Rybicki & Lightman 1979). However, in the limit when the photon energy is much less than the electron's rest energy ( $E'_i \ll m_e c^2$ , in the electron's rest frame), for typical collisions (initial and final angles  $\sim \pi/2$ ), the observed photon's final energy is

$$E_f \approx \gamma^2 E_i,$$
 31.

where  $\gamma = 1/\sqrt{1 - v^2/c^2}$  is the Lorentz factor. Since  $\gamma$  is always larger than unity for relativistic electrons, photons can gain energy by factors of several after a single scattering.

#### Thermal Comptonization

Inverse Compton scattering can take place when the UV or soft X-ray photons from the thermal disk undergo multiple scatterings in a hot ( $\sim 10^9 \, \mathrm{K}$ ) and optically thin ( $\tau \sim 1-3$ ) X-ray corona, which explains the power-law X-ray continuum observed from accreting black holes (Sec. 3.1.2). The cutoff at high energies is related to the electron temperature of the plasma.

# **Bulk Motion Comptonization**

If electrons are accelerated to nearly the speed of light by non-thermal processes (such as in the accretion flow inside the ISCO radius, or through strong magnetic fields) and have trans-relativistic bulk motions, they can still upscatter photons to a hard non-thermal distribution, even if the electrons are cold (Blandford & Payne 1981, Chakrabarti & Titarchuk 1995). In this case, the plasma can have a lower temperature and lower optical depth than in the thermal Comptonization picture.

3.1.2. The ubiquitous hard X-ray corona: Phenomenology. Coronal X-ray emission provides crucial insights into the energetic processes near supermassive black holes, as it probes the innermost regions and thus it is key to understanding AGN emission, black hole feedback, and galaxy evolution. Observationally, the X-ray continuum from most Seyfert AGN is described by a power-law with photon index  $\Gamma$  and an exponential cutoff at high energies

 $(E_{\rm cut} \sim 300\,{\rm keV})$ . Physically, this is interpreted as the result of soft UV disk photons entering a hot  $(T \sim 10^9\,{\rm K})$  and optically-thin  $(\tau \sim 1-3)$  corona. Low-energy photons gain energy through multiple inverse Compton scatterings with hot electrons, producing a power-law continuum, in a process commonly known as *Thermal Comptonization* (see Sidebar entitled *Origin of the Power-law Continuum*). The energy gained by the coronal photons is limited by the mean kinetic energy of the relativistic electrons, and thus the power law falls off abruptly at a cutoff energy  $(E_{\rm cut})$  of a few times the electron temperature of the plasma (Titarchuk & Lyubarskij 1995).

Observationally, it is relatively straightforward to measure the slope of the continuum  $(\Gamma)$  and its cutoff at high energies  $(E_{\text{cut}})$ . With these quantities, one can derive the electron temperature  $(T_e)$  and optical depth  $(\tau)$  of the corona by implementing the empirical relationships: <sup>4</sup>

$$E_{\rm cut} = (2-3)kT_e, 33$$

where the exact value of the proportionality constant depends on the assumed coronal geometry (Petrucci et al. 2001), and

$$\Gamma = -\frac{1}{2} + \sqrt{\frac{9}{4} + \frac{1}{\theta_e \tau (1 + \tau/3)}} : \tau \gtrsim 1,$$
 34.

where  $\theta_e = kT_e/m_ec^2$ , and  $m_ec^2 = 511 \,\mathrm{keV}$  is the electron's rest mass energy (Pozdnyakov et al. 1983, Lightman & Zdziarski 1987, Haardt & Maraschi 1993). From these relationships, it is clear that objects with  $\Gamma \sim 2$  are unlikely to have coronal temperatures above  $\sim 100 \,\mathrm{keV}$ , which implies observed cutoffs of  $E_{\mathrm{cut}} \sim 300 \,\mathrm{keV}$  (Figure 3, left).

Systematic studies with the Swift/BAT sample suggest higher accretion rate AGN exhibit steeper photon indices and cooler coronae (e.g.; Ricci et al. 2018, Hinkle & Mushotzky 2021), but follow-ups with smaller NuSTAR samples have not confirmed these correlations (e.g.; Tortosa et al. 2018, Kamraj et al. 2022, Serafinelli et al. 2024). This discrepancy may stem from NuSTAR's narrower energy range (3–79 keV) and smaller sample sizes, though its higher signal-to-noise allows better parameter estimation by disentangling degeneracies between the continuum slope ( $\Gamma$ ) and high-energy cutoff ( $E_{\rm cut}$ ). Correlations between coronal parameters and accretion rate reflect the complex interplay between heating and cooling mechanisms. For example, higher accretion rates should increase UV photons cooling the corona, steepening  $\Gamma$  and lowering  $E_{\rm cut}$  (Kara et al. 2017). A lack of correlation between  $\Gamma$  and  $E_{\rm cut}$  with accretion rate could point towards a more complex physical scenario beyond the simple thermal Comptonization picture.

In fact, an important caveat to the present discussion is that historically only thermal Comptonization has been assumed as the physical origin of the corona. However, as we explore in the next Section, new research on relativistic plasma physics is rapidly changing this picture, pointing towards *Bulk Motion Comptonization* as an alternative scenario (see Sidebar entitled *Origin of the Power-law Continuum*). This could dramatically change the

$$\Gamma = 1 + \frac{-\ln \tau + 2/(3 + \theta_e)}{\ln 12\theta_e^2 + 25\theta_e},$$
32.

(Sridhar et al. 2020).

 $<sup>^4</sup>$ Eq. 34 is appropriate for most cases, sources with faint and/or soft non-thermal emission might indicate emission from a corona with much lower optical depth ( $\tau < 1$ ), in which case an alternative expression should be used, e.g.,

physical inferences derived from X-ray observations (e.g.; with temperature really being driven by the kinetic energy of bulk motion in some cases).

3.1.3. The ubiquitous hard X-ray corona: Its origin and geometry. The physical origin of the X-ray corona remains an active area of research. The presence of compact radio emission in most AGN (Smith et al. 2020) has led to suggestions that the magnetic fields responsible for jet emission could also confine and heat the corona (Behar et al. 2018, King et al. 2017). Such a correlation between the corona and the jet is obvious in black hole X-ray binaries, where persistent radio jets are only observed in "hard" accretion states, during which the coronal continuum dominates the X-ray spectrum (Fender et al. 2004, Markoff et al. 2005). Other models do not require the corona to be the jet base. For example, 3D radiation MHD simulations of sub-Eddington disks by Jiang et al. (2019b) show a fairly hot ( $\sim 10^8$  K), optically-thin and spatially compact (within  $10R_g$ ) plasma that resembles the X-ray corona. More recently, Bambic et al. (2024) demonstrated through shearing box simulations that vertical magnetic fields could efficiently power coronae in bright AGN and quasars without necessarily launching a strong jet. For further details on the role of magnetic fields in jets, disks, and coronae, see Davis & Tchekhovskoy (2020) and references therein.

Constraining the geometry of the X-ray corona, such as its size and location, is vital for testing different corona formation models. For instance, the original "two-phase" model predicts a corona extending over the disk (Haardt & Maraschi 1991), while the jet-base model suggests a compact corona, confined to within  $\sim 10R_g$  (Ghisellini et al. 2004). Microlensing and reverberation studies of quasars (Sec. 3.5.1) have offered promising constraints on the size of the corona, indicating that it is centrally located and is confined to within tens of  $R_g$ , and is more compact than the optically-emitting accretion disk (e.g.; Pooley et al. 2007, De Marco et al. 2013, Mosquera et al. 2013, Uttley et al. 2014). This has led to the adoption of the lamp-post geometry, where the X-ray corona is approximated by a point source above the accretion disk, potentially arising from shocks in an ejection flow or the base of a jet (e.g.; Matt et al. 1991, Martocchia & Matt 1996, Miniutti & Fabian 2004). More realistic 3D coronal geometries are now being considered in recent research (e.g.; Wilkins et al. 2016, Gonzalez et al. 2017, Zhang et al. 2019).

Although the lamppost geometry is highly idealized, it allows for a more simple calculation of the illumination pattern of the accretion disk by using photon ray-tracing codes in full general relativity. The predicted illumination profile is in turn incorporated in X-ray disk reflection and reverberation models which are widely used to constrain properties of the inner disk and estimate the black hole spin (see Sec. 3.4 on reflection and spin measurements, and Sec. 3.5.1 on reverberation). So even though the exact origin of the corona is not settled, we can use the corona to shine a light on the accretion disk closest to the event horizon.

**3.1.4.** The ubiquitous hard X-ray corona: The microphysics and pair thermostat. As discussed in the previous section, the exact physical origin of the X-ray corona is still a matter of research. More consensus exist on the microphysics of the corona. The temperature of the plasma is set by the balance of heating and cooling. Heating has traditionally been attributed to magnetic reconnection (e.g.; Galeev et al. 1979, Merloni & Fabian 2001, Sironi & Beloborodov 2020). However, if this were the only heating mechanism, X-ray coronae would be short-lived because Compton cooling has a much shorter timescale (Beloborodov 2017). Thus, recent works on particle-in-cell (PIC) simulations point to a more complex

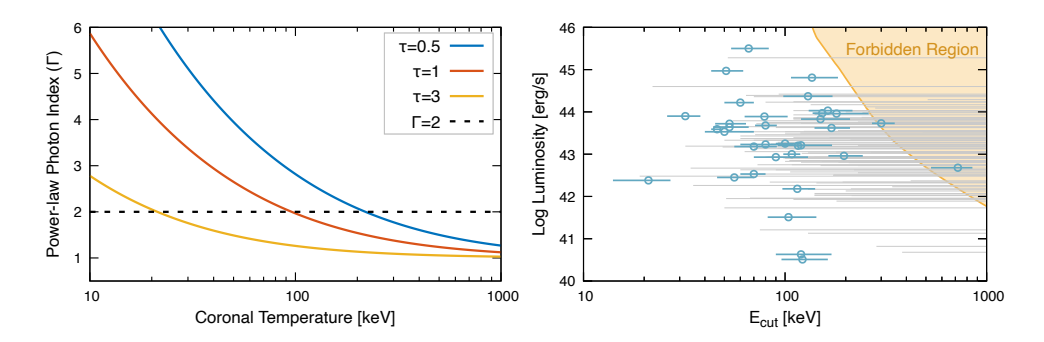


Figure 3

Left: Photon index  $\Gamma$  as a function of coronal temperature for constant optical depths computed with the relationship from Eq. 34. If the slope of the continuum (i.e.;  $\Gamma=2$ , black-dashed line), and the electron temperature is derived from the cutoff energy (Eq. 33), one can easily estimate the optical depth of the corona. Right: Compilation of measured coronal temperatures and luminosities for local AGN from Bertola et al. (2022). Formal constraints are shown with blue-empty circles, while lower-limits are shown as thin-gray bars. The pair-production forbidden region assumes a slab geometry in a  $10^8 M_{\odot}$  black hole (different geometries and masses define slightly different regions, for more details see, Kammoun et al. 2024a).

scenario, in which relativistic bulk motions of a colder plasma can efficiently Comptonize seed photons to high energies (e.g.; Sridhar et al. 2021, 2023, Gupta et al. 2024). These simulations also show that turbulence in a highly magnetized plasma can explain state transitions in stellar-mass black hole systems, when all relevant quantum electrodynamical processes are considered (Nättilä 2024).

Compton cooling is driven by the number of high-energy photons escaping the corona, which gained energy via inverse Compton scattering<sup>5</sup>. Even a small number of such photons produce copious amounts of electron-positron pairs to share the available thermal energy, effectively cooling the electrons until a balance is reached. This is known as the *pair-production thermostat model*. The maximum temperature allowed is directly related to the total X-ray luminosity of the corona. The inverse Compton cooling power is given by

$$P_{\rm IC} = \frac{4}{3} \sigma_{\rm T} c \beta^2 \gamma^2 U_{\rm rad}, \qquad 35.$$

where  $\sigma_{\rm T}$  is the Thomson cross section,  $\beta$  is the velocity of the electrons (in units of c),  $\gamma$  is the Lorentz factor, and  $U_{\rm rad}$  is the energy density of the radiation field incident to the corona. Thus, brighter disks will tend to cool the corona more efficiently<sup>6</sup>, possibly faster than the mechanism responsible for the heating. In such a situation, the plasma will be out of thermal equilibrium, which leads to an energy imbalance, effectively quenching the coronal emission. This could very well be the reason why the coronal continuum in black hole binaries quickly becomes much softer and fainter when sources transition from the hard

<sup>&</sup>lt;sup>5</sup>In general, electron scattering is a very "socialist" process; the particle with more energy shares it with the less energetic one. Thus, photons will gain or lose energy depending on their relation to the kinetic energy of the electrons.

<sup>&</sup>lt;sup>6</sup>Formally, an effective cooling requires  $U_{\rm rad}$  to be large, and thus the important quantity is the number of photons per unit volume.

to the soft state (e.g.; Sridhar et al. 2020). However, it is unclear whether AGN undergo similar state transitions (just over very long time scales), or whether such a behavior is exclusive to stellar-mass black hole systems.

The right panel in Figure 3 shows the most recent coronal temperature estimates and their X-ray luminosity (2 –  $10\,\mathrm{keV}$ ) from the compilation of Bertola et al. (2022), which follows the work of Fabian et al. (2015). Many of these measurements are lower limits, owing to limitations in current detectors. As most temperatures are in the range of  $10^8$  –  $10^9$  K, this requires the detection of cutoff energies of hundreds of keV, while current hard X-ray telescopes like NuSTAR are only sensitive up to  $\sim 80\,\mathrm{keV}$ . However, these measurements generally agree well with the predictions from the pair-thermostat model. Crucially, none of the well determined temperatures are observed to violate the theoretical limit (Fabian et al. 2015, and see Kammoun et al. 2024a for a recent review).

Another important aspect to note from Fig. 3 is that we do not observe a conglomeration of points at the thermostat limit, which is expected if the plasma is assumed to be composed of electrons following a purely thermal distribution of energy. Instead, several AGN are reported at much lower electron temperatures (e.g.; Baloković et al. 2015, Ursini et al. 2016, Kara et al. 2017, Tortosa et al. 2018, Reeves et al. 2021). This spread of coronal temperatures may be indicative of bulk motion Comptonization or of a plasma with a mixture of thermal and non-thermal particles (a so-called *hybrid plasma*), as suggested by several authors (e.g.; Ghisellini et al. 1993, Zdziarski et al. 1993, Fabian et al. 2017). Understanding whether the corona is indeed a hybrid plasma has consequences for how it is powered through magnetic dissipation processes (i.e., via magnetic reconnection, instabilities, and turbulence; Spitkovsky 2005, Comisso & Sironi 2018, Sironi & Spitkovsky 2014). Thus, the observational characterization of X-ray coronae and their properties probes fundamental plasma physics.

#### 3.2. Polarization Properties of the X-ray Continuum

X-ray polarization has recently made an appearance in the high-energy astrophysics community with the launch of the Imaging X-ray Polarimetry Explorer (IXPE; Weisskopf et al. 2022) in December 2021. In general, linear polarization of light—in any energy band—measures the direction of the electric field vector, such that the degree of polarization (PD; often also denoted as  $\Pi$ ) indicates the fraction of the intensity emitted in a preferential direction, while the polarization angle (PA; or  $\Psi$ ) indicates what that direction is.

Polarimetry observations of accreting black holes offer the opportunity to learn more about the geometry and morphological configuration of the regions emitting in X-rays. For radio-loud AGN, strong polarization is observed from the synchrotron jet emission. Conversely, radio-quiet AGN are environments relatively clean from synchrotron radiation and thus their polarization signal, albeit fainter, allows the study of accretion processes. In unobscured, Type 1 AGN, most of the polarization is likely taking place in the X-ray corona, driven by electron scattering, and thus measuring the PD and PA provides direct constraints on its geometry. In obscured AGN, polarization measurements can be used to describe the orientation of the obscuring torus (Ursini et al. 2023).

Theoretical models predict several different possible geometries for the X-ray corona—including configurations such as spherical, conical, slab, or patchy—which will produce different polarization signals. In particular, the PA indicates the orientation of the corona, while the PD, and its dependence on energy, can discriminate between different model

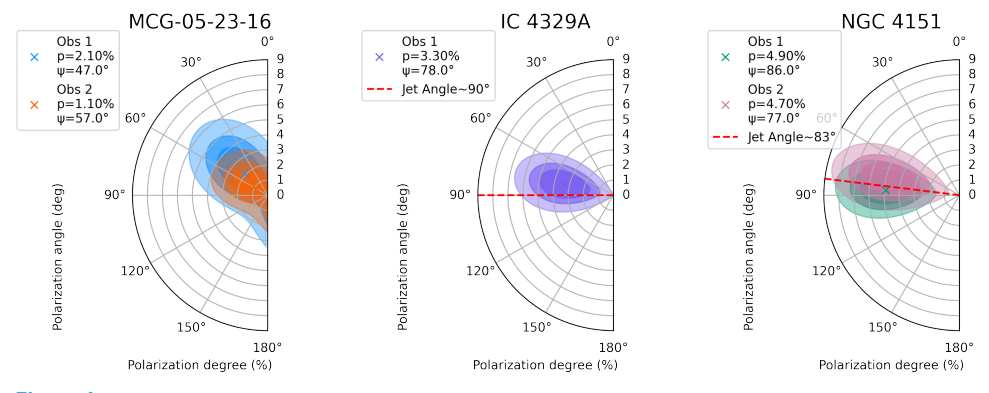


Figure 4

X-ray polarization measurements for the three Type 1 radio-quiet AGN observed to date by IXPE. For each source, a protractor plot shows the polarization degree and polarization angle in the  $2-8\,\mathrm{keV}$  band using contours at 1, 2, and  $3-\sigma$  confidence levels. Individual observations for each source are shown with different colors. The orientation of a radio jet is shown for the two sources with reported estimates (red-dashed line). Original version of the Figure courtesy of Swati Ravi (MIT).

flavors (e.g.; Poutanen & Svensson 1996, Veledina & Poutanen 2022). For example, the relativistic outflowing plasma model proposed by Poutanen et al. (2023) predicts a different dependency of the PD with energy for varying velocities of the scattering medium.

As of the writing of this Review, IXPE has conducted observations of three Type 1 AGN: MCG-05-23-16 (Marinucci et al. 2022, Tagliacozzo et al. 2023), IC 4329A (Ingram et al. 2023), and NGC 4151 (Gianolli et al. 2023), though NGC 4151 is formally a Type 1.9, i.e. with significant line-of-sight obscuration. Their measured PA and PD are shown in the protractor plots in Figure 4 for different confidence levels. A significant PD is seen only in NGC 4151 at 1-8%, which indicates scattering in the corona in this system. The PA of NGC 4151 and IC 4329A appear aligned with the jet (though the PD of IC 4329A is consistent with zero at the  $3\sigma$  confidence level). A significant PA aligned with the jet would suggest that the corona is extended along the disk plane, and perpendicular to the jet. While the AGN measurements remain tentative, similar measurements of alignment of the PA and jet have been seen in BH X-ray binaries, such as Cyg X-1 (Krawczynski et al. 2022) and GX 339-4 (Mastroserio et al. 2024).

At face value, the *IXPE* measurements of Type 1 AGN challenge the results from microlensing and reverberation, which show the X-ray corona is more compact than the disk (Section 3.1.2), and also challenge the simplest lamppost geometry for the corona, widely used in X-ray reflection measurements (Section 3.4). It appears that, in addition to deeper *IXPE* observations of a larger sample of truly unobscured AGN, we require self-consistent modeling of spectra, timing and polarization with more sophisticated treatments of the corona (e.g., including also some radial extent of the corona, or a bulk outflow velocity). At this point, it is thus safe to argue that further observational and theoretical efforts are needed to reconcile these predictions.

More details on these measurements and those on Type 2 AGN can be found in the recent review by Marin et al. (2024), and references therein. A similar review for black hole X-ray binaries is given by Dovčiak et al. (2024), and a discussion comparing polarimetry

# 3.3. Variability Properties of the X-ray Continuum

Rapid variability is one of the hallmark features of an AGN, and, as discussed in Section 1.1, allowed for the early realization that these enormous luminosities were powered by accretion on to a central supermassive black hole (Lynden-Bell 1969).

AGN timing analysis is difficult because the observed variability is stochastic (or random). This is demonstrated for four example AGN light curves in Fig. 5, all observed with the *XMM-Newton* observatory for 20 hours (or 70 ks in X-ray parlance). Unlike deterministic analyses, like the modeling of energy spectra from a non-variable sources or the timing of a strictly periodic sources, where the analysis is repeatable within the limits of measurement noise, AGN variability is unpredictable, and the signal itself is a noisy process. The ups and downs of an individual AGN light curve are not particularly meaningful: they are simply a random realization of an inherent underlying physical process. Therefore, for such non-deterministic data, statistical handling is required. One gains physical insights by determining the average, underlying variability properties (see Vaughan et al. 2003 for a beautiful pedagogical review of different tools for studying aperiodic variability).

So, what are these underlying physical processes? Over the decades, much theoretical work has gone into understanding the variability processes at play in AGN. In recent years, radiation MHD simulations can even be run long enough to also participate in these studies, and promising work is beginning to reproduce the observed variability from first principles (Hogg & Reynolds 2016, Turner & Reynolds 2023, Secunda et al. 2024). To date, we still do not fully understand all the complex variability processes at play, but in short, the variability can generally be described by the theory of "propagating fluctuations" (Lyubarskii 1997). Fluctuations in the disk's surface density are driven by the interaction between magnetic fields and differentially rotating gas (known as MRI; Balbus & Hawley 1998). These local fluctuations occur at all radii in the disk, and then evolve through the disk at the local viscous time (Eq. 10). Fluctuations originating in the outer, cooler disk produce slower, lower-energy flares and then propagating inwards, later modulating the variability of faster, hotter independent flares from the innermost regions. The stochastic light curve we observe is then due to the response of the accretion flow and corona to these intrinsic fluctuations (Mummery & Turner 2024, Uttley & Malzac 2023).

Here we review the basic properties of X-ray variability in AGN and compare to what is seen at longer wavelengths. We do not attempt to summarize all the rich phenomenology, but instead highlight some key observables that help us infer physical properties, like the black hole mass and accretion flow viscosity, geometry, and dynamics.

**3.3.1.** X-ray variability estimates the black hole mass. Even from very early X-ray observations of AGN light curves (Barr & Mushotzky 1986), it was recognized that luminous AGN showed less variability than their lower luminosity counterparts. Now, we understand this observation as largely due to the fact that the characteristic variability scales with the black hole mass (Fig. 1). The dependence can be seen anecdotally in Fig. 5-left, where we compare the XMM-Newton  $0.3 - 10 \,\text{keV}$  light curves of four nearby Seyfert 1s, spanning roughly four orders of magnitude in mass from  $10^5 \, M_{\odot}$  to  $10^8 \, M_{\odot}$ . In a 70 ks (20 hr) light curve, the largest black hole (Ark 120) shows variability on timescales of a few hours (corresponding to roughly the dynamical timescale for a  $10^8 \, M_{\odot}$  black hole, Eq. 25), whereas

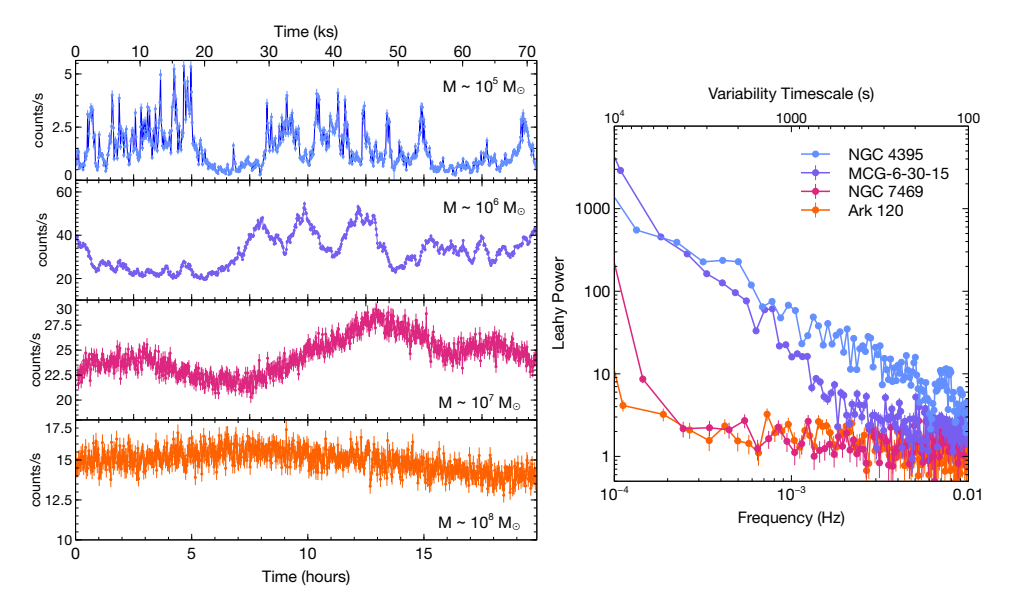


#### Figure 5

Left: A comparison of the X-ray light curves of four representative AGN with masses of  $10^5 M_{\odot}$  (top) to  $10^8 M_{\odot}$ , measured with XMM-Newton on timescales of hours. AGN vary stochastically, with smaller black holes varying more rapidly than larger. As such, the X-ray variance over a particular timescale is a strong indicator of the black hole mass (Ponti et al. 2012). Right: The corresponding PSDs for the same AGN. In the high frequency regime probed by XMM-Newton ( $\nu \sim [10^{-5} - 10^{-2} \, \text{Hz}]$ ), AGN show a red noise power spectrum ( $\alpha \sim 2$ ) that becomes dominated by Poisson noise at high frequencies. Lower mass black holes show power up to higher frequencies. For AGN that are roughly  $10^6 M_{\odot}$ , we observe variability power above the Poisson noise limit on timescales roughly close to the thermal and viscous timescales (see Fig. 1).

for the same duration light curve, a  $10^5~M_{\odot}$  black hole (NGC 4395) shows variability on timescales as short as tens of seconds. In other words, for the same duration light curve, the smaller black hole probes variability on the thermal, viscous, and dynamical timescales.

In a systematic study of Type 1 (unobscured) AGN in X-rays, Ponti et al. (2012) showed this behavior is common: the excess variance (a measurement of the intrinsic variance, where measurement noise is subtracted off) scales with the mass of the black hole on the timescales probed in a typical XMM-Newton observation. As such, measuring the amount of X-ray variability is a relatively inexpensive way to estimate AGN masses. This has recently been confirmed in a larger number of sources across a larger luminosity range, and out to high redshifts (Elías-Chávez et al. 2024, Prokhorenko et al. 2024).

**3.3.2.** The X-ray and UVOIR power spectral densities. One of the most common tools for quantifying the average AGN variability properties is the power spectral density (PSD), which is a measure of the variability power (the mean of the squared amplitude) as a function of temporal frequency, 1/timescale (Green et al. 1993, Lawrence & Papadakis 1993). This is a powerful tool for measuring how turbulence builds up in the accretion flow of standard AGN. Moreover, recently, large scale time domain surveys have been used to search for

periodic or quasi-periodic signals from exotic transients (e.g., from binary supermassive black hole, or other orbiting objects, see Sections 4.3 and 4.4). In order to definitively find these exotic outliers, it is vital first to have robust understanding of the variability behavior of individual AGN across different masses and accretion states. Here, we review the X-ray and optical PSD properties of standard AGN.

Fig. 5-right shows the corresponding X-ray PSDs for the four AGN light curves to the left. Seyfert 1s typically show high-frequency PSDs that are well described as a power-law, where the variability power P(f) scales with frequency f as  $P(f) \propto f^{-\alpha}$ . AGN light curves typically show so-called "red noise" power spectra, where the power-law slope of the PSD,  $\alpha$ , is > 1. In a systematic study, González-Martín & Vaughan (2012) found that X-ray PSDs of Seyfert 1s in the frequency range of  $10^{-5}$  Hz to  $10^{-2}$  Hz (describing rapid variability from minutes to  $\sim 1$  day) are generally consistent with  $\alpha \sim 2$  (so-called "random walk" noise), albeit with large scatter across sources. Two light curves of the same AGN in a given accretion state will look different because of statistical fluctuations (inherent to any stochastic process), but their power spectra will be the same if they arise from the same underlying physical process.

The X-ray variability power does not keep rising indiscriminately at longer timescales, and instead at some frequency (the so-called break frequency), we observe a turn-over to a shallower slope. This break frequency scales with mass and accretion rate in AGN and even down to stellar-mass black holes (McHardy et al. 2006). While the origin of the break frequency is unknown, it marks the timescale above which variability is produced less efficiently. This timescale has been associated with the viscous timescale at the inner edge of an optically-thick disk (e.g., a  $10^6 M_{\odot}$  AGN may show a break frequency of  $10^{-5}$  Hz or 27 hrs, which is roughly the viscous timescale at the ISCO of a non-rotating black hole, Eq. 10). The break frequency has alternatively been associated with the cooling timescale of electrons in the Comptonization model (Ishibashi & Courvoisier 2012).

Complimentary optical studies on sub-day timescales have been challenging, but the Kepler exoplanet-discovery mission did provide long uninterrupted light curves at high cadence (especially during its K2 mission phase), thus allowing for similar variability analysis on the same timescales as typically probed in the X-rays. The high-frequency optical PSDs from Kepler exhibit lower normalizations and steeper power-law slopes than X-ray PSDs (e.g.  $\alpha = [2.6-3.3]$ ; Mushotzky et al. 2011, Edelson et al. 2014, Smith et al. 2018), and are inconsistent with expectations from the random walk ( $\alpha \sim 2$ ) seen at X-rays. Similar conclusions are drawn from longer timescale simultaneous X-ray, UV and optical monitoring campaigns from Swift, as shown for the AGN NGC 5548 in Fig. 6 (adapted from Panagiotou & Walter 2020). While X-rays often vary by > 50% day-to-day, the variability amplitude decreases to  $\sim 20\%$  in the UV, and < 10% in the optical. Simply put: optical/UV light curves do not show as rapid variability as X-rays, indicating that the X-ray corona is more compact than the optical/UV-emitting disk.

In recent years, with the increasing time baseline and footprint of large all-sky optical time domain surveys, these studies can be expanded to large samples of AGN. While the sampling is poorer than in targeted campaigns, the number of AGN is enormous, and careful stacking shows that the optical PSD slope above the break is 2.5-3 (Arévalo et al. 2023). This rejects the commonly used DRW model. Similar to earlier X-ray studies, these authors find that the optical PSD amplitude decreases and slope steepens with increasing mass and Eddington ratio (Arévalo et al. 2023, Petrecca et al. 2024). This is perhaps related to the fact that the X-ray to bolometric luminosity ratio decreases with increasing

**DRW:** Damped Random Walk, PSD with  $P(f) \propto f^{-2}$ that breaks to flat slope at long timescales.

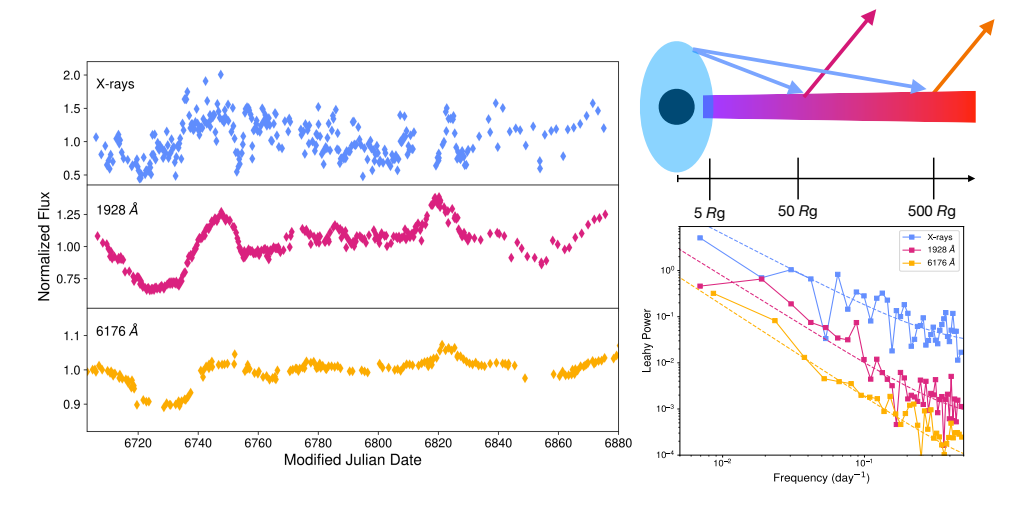


Figure 6

Left: A comparison of the X-ray light curve (blue) to longer wavelength UV (pink) and optical (yellow) for the AGN NGC 5548. The X-rays are most rapidly variable, and originate at smallest scales (within  $10~R_g$  of the black hole). The UV and optical originate further out in the accretion disk. Most of the rapid variability observed in this  $\sim$  1-year campaign is much too fast to be driven by changes in the mass accretion rate through the disk (Eq. 10), but rather is due to irradiation of the disk by the highly variable X-ray corona. This irradiation from a central source explains why the UV and optical are delayed with respect to the X-rays (See Section 3.5.1), and why the UV and optical power spectra (bottom-right) are steeper and lower normalization than the X-ray PSD (Section 3.3). On the longest timescales, variability due to mass accretion rate fluctuations may also contribute in some cases (e.g., see Hernández Santisteban et al. 2020, Hagen et al. 2024). Light curves and PSDs for NGC 5548 courtesy of Christos Panagiotou (MIT).

Eddington ratio (see Section 3.1.1), and as such, higher luminosity AGN do not have enough X-ray emission to modulate the UV variability. Moreover, the disk temperature increases with mass accretion rate (Eq. 11), and thus a fixed optical bandpass probes larger radii for higher accretion rates. Emission originating from a larger radius (i.e. larger emitting region) will naturally be less variable. This may be an important point in predicting the rest-frame UV variability of Little Red Dots, if indeed they are super-Eddington AGN (e.g. Pacucci & Narayan 2024).

Studies of the broadband noise properties of power spectra have largely been phenomenological, but there are promising physical models that attempt to self-consistently explain the variability across different energy bands (Papadakis et al. 2016), e.g., by predicting how the X-ray variability from the corona is damped out as it irradiates the accretion disk producing reprocessed UV variability (Panagiotou et al. 2022b). These types of physical models will become more constraining with the launch of missions like *ULTRASAT*, providing unprecedented high-cadence UV light curves on timescales of days to minutes for a large number of AGN.

**3.3.3. Low-frequency hard lags are ubiquitous.** Long timescale hard-band lags are another fundamental property of accreting black holes, and encode information about the continuum

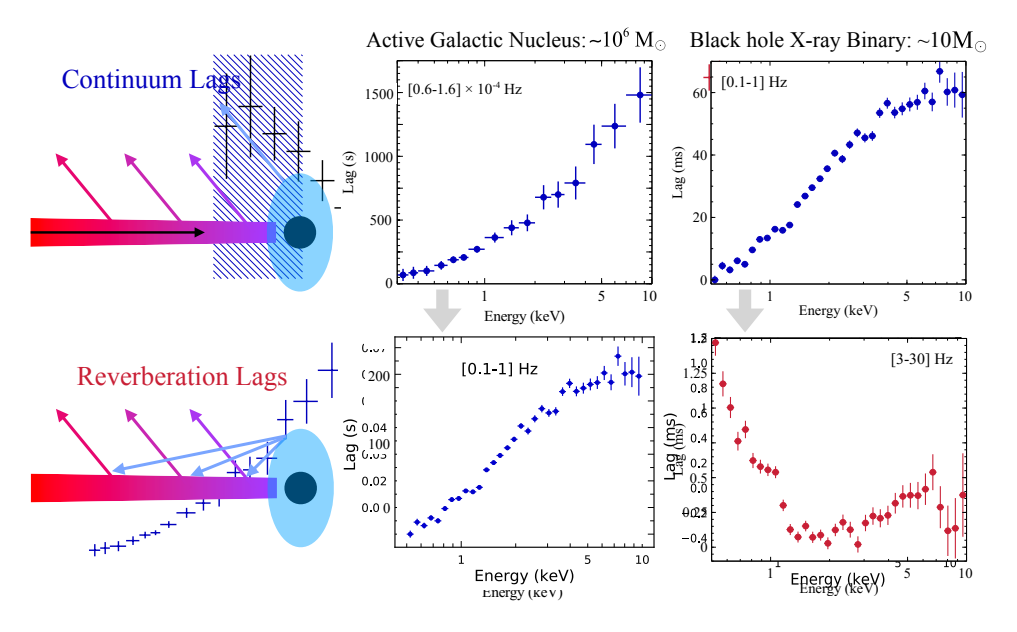


Figure 7

A comparison of the frequency-resolved time lags for the  $\sim 10^6~M_{\odot}$  AGN Ark 564 (middle column), compared to the black hole X-ray binary MAXI J1820+070 with a  $\sim 10~M_{\odot}$  black hole. The "low-frequency" lags (top row) show a featureless log-linear increase with energy, and are understood to be due to mass accretion rate fluctuations propagating through the disk and into the corona. At high frequencies (bottom row), we observe a distinctly different dependence on the lags with energy. These lags are instead understood as due to reverberation, as the corona irradiates the cooler disc (Section 3.5.1 for details). The lags in luminous Seyferts look very similar to the lags in the luminous hard state of accreting stellar mass black holes, supporting the idea of mass invariance in accreting black holes (see Sidebar entitled Stellar-mass Black Holes for details).

source (Fig. 7-left). In the context of AGN, 'long' timescales are  $\sim 5 \times 10^{-5} c/R_g$  (or  $10^{-5}$  Hz for a  $10^6 M_{\odot}$  black hole). The observed hard-band lags were originally discovered in black hole X-ray binaries (Miyamoto & Kitamoto 1989, Nowak et al. 1999), and later discovered in AGN (Papadakis et al. 2001). In Kara et al. (2016), we showed that these hard lags were a ubiquitous feature in unobscured AGN systems.

Because the variability is rapid, and a single uninterrupted observation with, for instance, XMM-Newton can capture a range of variability timescales, time lags in X-rays are most commonly studied in the Fourier domain (see Nowak et al. 1999, Uttley et al. 2014 for descriptions of the technique). Whereas the cross-correlation function (traditionally used in optical studies) provides a measurement of the time lag averaged over all variability timescales, the Fourier approach allows for the measurement of different timescales at different temporal scales. The benefit of this approach is that it allows one to measure lags from different physical mechanisms that dominate the variability at different timescales. For instance, in a standard unobsured AGN, when we zero in on the long-timescale variability (low-frequency), we observe the hard X-rays lagging behind the soft X-rays, but when isolating the short-timescale variability (high-frequency), we see the opposite—the soft X-rays lagging the hard. These high-frequency soft lags are interpreted as due to reverberation

echoes, which will be discussed in Section 3.5.1, but for now, we want to make the point that these two different physical lags can only be "teased out" of the data when using the frequency-resolved Fourier analysis, whereas a standard cross-correlation analysis averages over all variability timescales, and thus would only measure the low-frequency hard lags that dominate the variability power.

When isolating variability on long timescales, we observe a featureless log-linear increase in time lag with energy, indicating that this is a property of the continuum emission. Kotov et al. (2001) first explained these lags within the context of the propagating fluctuations model: Mass accretion rate variations produced in the outer, cooler parts of the disk propagate inwards, leading to correlated, and delayed emission from fluctuations from the closer-in, hotter portions of the disk. The greater the difference in energy, the longer the lag, as the propagation front travels a larger distance through the disk. Arévalo & Uttley (2006) expanded these studies, and demonstrated that the same model developed for black hole X-ray binaries can apply to AGN, assuming that the corona tracks the variability of the thermal seed photons. It is unlikely that the observed lags are due to fluctuations that propagate through the corona itself, as the propagation timescale through the optically-thin corona is much shorter than the viscous timescale through the disk. Recently, Uttley & Malzac (2023) demonstrated that fluctuations propagating through the disk increase the seed-photon flux entering the corona, thus cooling it, which leads to a steeper powerlaw shape, and as its re-heated (via e.g. magnetic reconnection) the spectrum hardens again. The result is a pivoting of the slope of the continuum spectrum as it fluctuates in luminosity. which leads to hard-band lags (e.g.; Ingram et al. 2019).

As of recent years, global MHD simulations of accretion disks can now be run long enough to test such propagating fluctuations models (Hogg & Reynolds 2016, Turner & Reynolds 2023). They appear to rise from the magnetic dynamo. The amplitude and timescale of the variability is set by the microphysics of the accretion flow and the local viscous timescale. The simulations are beginning to reproduce observables like the PSD and the low-frequency hard lags (Turner & Reynolds 2023). In principle, by comparing observed variability properties to results of MHD simulations, we can probe properties of the accretion flow at the disk midplane that are otherwise unobservable.

# 3.4. X-ray Reflection Spectroscopy: A Probe of the inner accretion flow and black hole spin

For relatively luminous systems ( $L_{bol} \sim 0.01 - 0.3L_{\rm Edd}$ ) a fraction of the emitted photons irradiate the surface of the disk, producing a reflected emission component that contains a diverse range of atomic spectral features. Among these, the inner-shell transitions from Fe ions—predominantly the K $\alpha$  emission lines at  $6.4 - 6.97 \,\mathrm{keV}$  (depending on the ionization state)—together with a strong absorption K-edge around  $7 - 8 \,\mathrm{keV}$ , are typically the most prominent. Furthermore, reflection spectra exhibit a characteristic high-energy continuum, peaking at  $\sim 30 \,\mathrm{keV}$ , known as the Compton hump (George & Fabian 1991, Ross & Fabian 2005, García et al. 2020). Although the emission lines are narrow in the frame of the disk, once the accreting material approaches the ISCO, it is orbiting at relativistic speeds, while the emitted radiation experiences a strong gravitational redshift. These spectral components are shown in the top-left panel of Figure 8. Together, these effects both broaden and skew the emission lines from our perspective as a distant, external observer, resulting in a characteristic "diskline" emission profile (Fabian et al. 1989, Laor 1991, Brenneman &

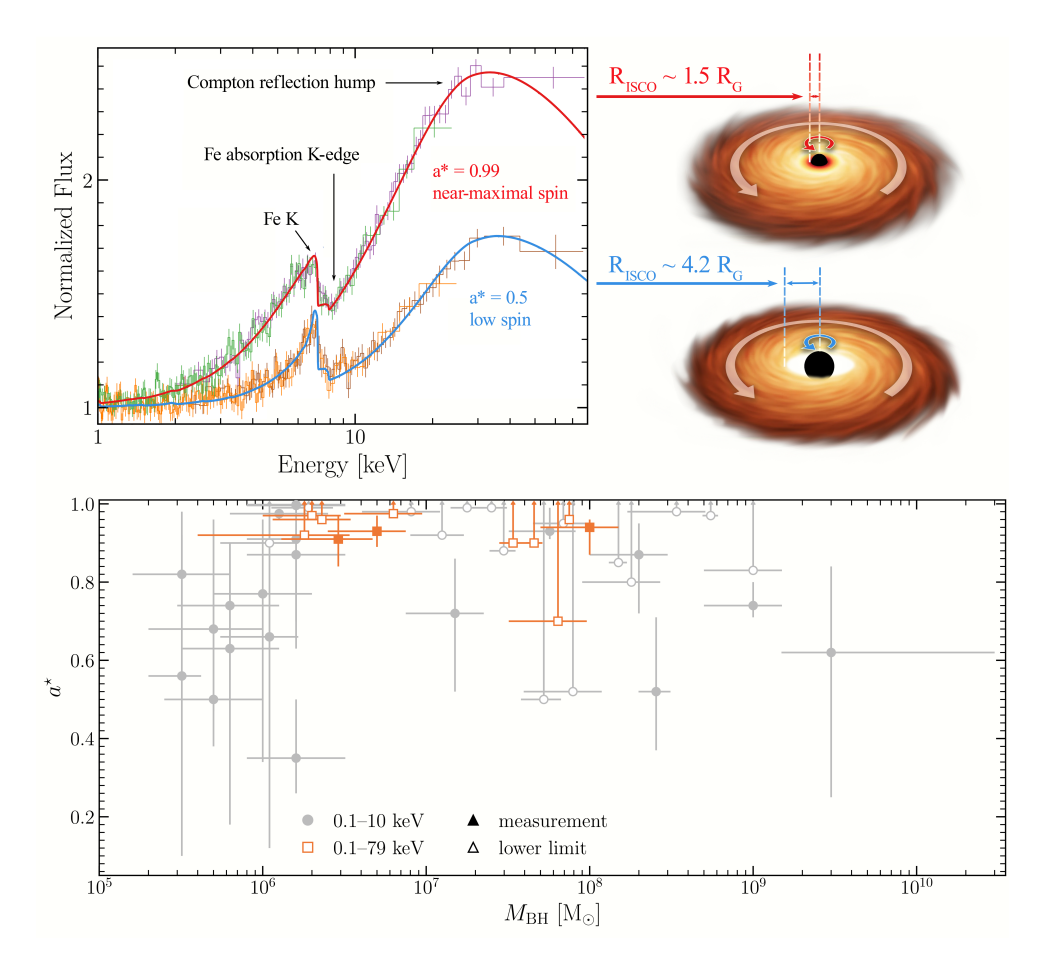


Figure 8

Top: Demonstration of the effects of the black hole spin on the accretion disk (right) and thus in the reflected X-ray spectrum (left). Relativistic frame-dragging effects cause the inner-edge of the disk to move closer in (i.e., lower  $R_{\rm ISCO}$ ) for rapidly spinning black holes, as shown in the artistic rendition on the right. The corresponding reflection spectra (left) from a XMM-Newton+NuSTAR observation simulated with the RELXILL model (Dauser et al. 2014, García et al. 2014) show the stronger distortion of the spectral features when the emission is produced closer to the black hole (high-spin case). Figure adapted from García et al. (2024). Bottom: Distribution of SMBH spins as a function of their mass constrained observationally using X-ray reflection spectroscopy. Filled and open symbols differentiate full constraints from lower limits. Orange and gray data points indicate measurements using a broadband ( $\sim 0.1-78\,{\rm keV}$ ) or soft-energy data only ( $\sim 0.1-10\,{\rm keV}$ ), respectively. Adapted from Piotrowska et al. (2024).

Diskline: Broad and asymmetric line profile emitted by a disk that is smeared by Newtonian and relativistic effects.

Reynolds 2006, Dauser et al. 2010).

Provided the disk extends down to the ISCO, as expected at moderately high accretion rates, then characterizing the relativistic blurring gives a measurement of  $R_{\rm ISCO}$ , and consequently provides an estimate for the black hole spin (Fig. 8, top-right). This can be done by virtue of the relationship between  $R_{\rm ISCO}$  and the dimensionless spin parameter

 $a_{\star} = Jc/GM_{\rm BH}^2$  (Bardeen 1970). The location of  $R_{\rm ISCO}$  changes by almost a factor of 10 between the two possible extreme spin values (i.e.;  $a_{\star} = \pm 0.998$ , for maximal prograde or retrograde spin, respectively; Bardeen et al. 1972, Thorne 1974).

There are a variety of methods to recover the black hole spin, but the so-called *relativistic reflection* model is the most successful method that can be reliably applied to AGN. While relativistic effects impact the entire reflection spectrum (Fig. 8, top-left), historically, this method is also referred to as the *Fe-line method*, as the K-shell iron emission is typically the strongest spectral feature.

In fact, broadband X-ray spectroscopy (beyond just fitting the iron line) is imperative for robust spin parameter constraints because the broadband continuum modeling (from  $\sim 0.3-50~\rm keV$ ) must be accurate (see Reynolds 2021, for a recent review). Now, since the launch of the hard X-ray telescope NuSTAR and in coordination with soft X-ray observatories, we have those broadband high signal-to-noise spectra, which has allowed for determination of black hole spin in a large fraction of AGN with such high S/N observations (Risaliti et al. 2013, Ricci et al. 2014, Wilkins et al. 2015, Jiang et al. 2018a, Walton et al. 2019).

Figure 8 (bottom) shows the current state-of-the-art of X-ray reflection spin measurements for AGN as a function of black hole mass, based on the most recent compilation of Piotrowska et al. (2024). This list of sources has been updated from the initial compilation of Reynolds (2021), which placed several quality criteria to select sources from all reported values in the literature. The current list contains 46 sources ranging over five decades in mass. For half of the sample, only lower limits can be imposed in their spin, given the limited signal of the data. Moreover, only 11 sources have spins measured over a broadband spectrum (i.e., including  $3-78\,\mathrm{keV}$  data from NuSTAR, where most of the reflection features are observed). Thus, it is possible that some of these measurements are biased, as they might depend strongly on the model fit to the soft energies only (i.e., fitting the soft excess with reflection; see Sect. 3.6).

The spin uncertainties shown in Figure 8 are only statistical, and do not include any possible systematic uncertainties inherent to the modeling of the reflection spectrum, which might include: accretion disk geometry, e.g., most models assume a razor-thin disk, while a vertical extension can influence the shape of the reflection signatures (Taylor & Reynolds 2018); physics of the accretion flow, which implies understanding the density profile in both vertical and radial directions (e.g., constant density vs. hydrostatic solutions vs. full radiation MHD simulations); and coronal geometry, which affects the illumination pattern produced by a simplified lamppost geometry vs. more realistic ones (e.g., Niedźwiecki & Życki 2008, Wilkins & Fabian 2012). See reviews by Reynolds (2021) and Bambi et al. (2021) for additional discussions. Nevertheless, accurate spins can be determined by analyzing multi-epoch and broadband observations of the same source, combined with careful comparisons of different model flavors (i.e., different geometries).

In the last few years, reflection models have become increasingly more physically motivated, e.g., by producing fully self-consistent models assuming a lamppost geometry (e.g.; Dauser et al. 2013), significantly improved microphysics by including high-density plasma effects in the atomic data and ionization calculations (García et al. 2016, Kallman et al. 2021, Ding et al. 2024), and other relativistic effects such as disk self-illumination (Connors et al. 2020), multiple reflections (Wilkins et al. 2020), returning radiation (Dauser et al. 2022), and both thermal (Mummery et al. 2024) and reflected (Dong et al. 2023) emission from the plunging region.

The relativistic reflection approach to measuring spin is particularly powerful because

it can be applied to black holes of all masses, not just in AGN (e.g.; Walton et al. 2012). Measuring spins in black hole X-ray binaries offers a way to test the systematic uncertainties of reflection modeling because in these lower mass systems, we have other methods for estimating black hole spin, the most well-studied of which is the so-called Continuum Fitting Method. In X-ray binaries, the accretion disks are so hot that they emit X-rays. Moreover, during an outburst, they conveniently transition to the "soft state", where the corona is weak, the disk dominates and we have a clean view of the Wein tail. By accurately measuring the thermal spectrum, we can estimate the inner radius of the disk, which, if associated with the ISCO, determines the spin (Zhang et al. 2019, McClintock et al. 2014). From the five systems for which both methods have been applied, there is agreement in all except one, GRO 1655–40, for which the constraint from reflection (> 0.9) is larger than that from the continuum fitting  $(0.7 \pm 0.1, \text{ see Table 2} \text{ in Reynolds 2021})$ .

Measuring the spin of stellar mass and supermassive black holes ultimately informs our understanding of the growth history of these black holes, and how much accretion via the disk can add angular momentum to the black hole over time (e.g., see Volonteri & Rees 2005 for AGN, and Fragos & McClintock 2015 for low-mass XRBs). The current sample of SMBHs is not yet sufficient to fully (and statically) discriminate among different evolutionary models for SMBH growth, nor does it provide enough constraints to directly inform cosmological simulations (Piotrowska et al. 2024), but the prospects are encouraging. The community faces the challenge of coordinating large observational campaigns in tandem with the most sophisticated reflection models to increase both the sample size and its accuracy.

# 3.5. Reverberation Mapping: A probe of the disk and corona geometry

3.5.1. X-ray Reverberation and the confirmation of the relativistic reflection model. The discovery of X-ray reverberation lags in AGN was a critical confirmation of the relativistic reflection model (Fabian et al. 2009, Zoghbi et al. 2010). One major prediction of the relativistic reflection scenario presented above is that the reflection spectrum should be delayed with respect to the continuum due to the additional light-travel path between corona and disk. This is similar to the general idea of optical broad line region reverberation lags, discovered in the 1980s, and which is commonly viewed today as our best means for measuring the masses of SMBHs (e.g., Peterson et al. 2004). In optical broad line reverberation mapping, one cross-correlates a light curve dominated by the primary continuum (in this case disk emission from hundreds of gravitational radii) and a light curve of the broad Balmer lines (produced via fluorescence of material further out in the BLR). Similarly, in X-rays, we search for the time delays between light curves dominated by the primary coronal continuum and those dominated by the reflection spectrum. As the emission lines in the X-ray spectrum are much broader than in the optical, this does add the additional complication that no band is purely continuum nor purely reflection. As such, careful modeling of the lags with general relativistic ray-tracing simulations is required to infer the geometry of the inner accretion flow (e.g., Cackett et al. 2014, Chainakun et al. 2016, Ingram et al. 2019). Moreover, in the X-ray band, the dominant time lag occurring on long timescales is the hard band lag (associated with the continuum and interpreted as due to propagating massaccretion rate fluctuations; see Section 3.3.3). One only directly observes the reverberation time delays by doing a Fourier de-composition to remove the low-frequency hard lags, and isolating the reverberation lags at high-frequencies (Uttley et al. 2014 and see Fig. 7).

While the timing technique and modeling is somewhat more complicated than required

in traditional optical BLR measurements, this technique has been successful in measuring X-ray reverberation lags in about two dozen sources that are bright enough, have sufficient rapid variability, and are not highly obscured (De Marco et al. 2013, Kara et al. 2016). For comparison, for a typical  $10^7 M_{\odot}$  black hole, one finds that the BLR light curve lags the continuum typically by  $\sim 1$  week (Cackett et al. 2021), corresponding to light-travel distances of centi-parsecs ( $\sim 10^5 \ R_g$ ). In X-ray reverberation, for a similar mass black hole, one measures time delays between the continuum and reflected light curves that are  $\sim 100$  seconds, corresponding to light-travel distances on the order of  $\sim 10 \ R_g$ .

The fact that one can self-consistently model both the time-averaged spectra and the time-dependence of those spectra was an important step in ruling out early competing models that suggested that the inner edge of the accretion disk was highly truncated and thus could not be used as an indicator of black hole spin (e.g. Mizumoto et al. 2014). In these alternative models, circumnuclear gas at hundreds/thousands of  $R_q$  from the black hole (perhaps from the inner BLR) caused absorption along our line of sight that could mimic the shape of a relativistically broadened iron line. However, such a model cannot explain the short lags associated with the soft excess and iron K line. Moreover, the same short lags are seen in black hole X-ray binaries, where there is a disk, but no a BLR (De Marco et al. 2017, Kara et al. 2019). The short X-ray reverberation lags confirm that the disk is not truncated, and that the X-ray corona is a distinct plasma confined above the surface of the disk. The reverberation results (e.g. Zoghbi et al. 2012, Kara et al. 2016) and the steep emissivity profile inferred from reflection spectroscopy (e.g. Jiang et al. 2019a) both suggest that the corona is radially confined to within  $\sim 10R_g$ , though recent IXPE observations appear to suggest somewhat greater radial extent (Sec. 3.2). Future modeling efforts that simultaneously model spectral, timing, and polarization data are required.

**3.5.2.** Connecting the X-rays to longer wavelengths. Because X-ray reverberation requires different telescopes, techniques, and models than traditional optical BLR reverberation mapping, these two fields developed in parallel for several years, but recently, there have been major efforts, like those of the AGN STORM 2 collaboration (Kara et al. 2021), to bring these communities together, to reverberation map the gas flows around AGN from the torus (as probed via IR; Landt et al. in prep.), down to the broad line region (with UV and optical spectroscopic; Homayouni et al. 2023), to the outer accretion disk (as probed via optical and UV continuum; Cackett et al. 2023), and all the way down to the ISCO (via X-rays; Lewin et al. 2024). For more details on each of these different reverberation techniques, and what they tell us about different scales of accretion, see the recent review by Cackett et al. (2021). Reverberation mapping from the torus to the ISCO is an enormous community effort, and the campaigns are very challenging to get all the data with as few observing gaps as possible, but when successful, they provide an unprecedented look at the lifecycle of an AGN: how gas flows funnel from the surrounding galaxy, through the disk and towards the black hole, and in doing so, launches outflows that may constitute the BLR itself, and may be powerful enough to affect the galaxies at large scales (see Section 3.8).

Multi-wavelength reverberation mapping campaigns from X-ray to NIR have been performed on roughly ten AGN, and while each AGN has its own idiosyncrasies, a few general results have been found: In all cases, the optical lags behind the UV, following the functional form that the time lag  $\tau \propto \lambda^{4/3}$ , as expected for irradiation of a disk around a centrally-located ionizing source (e.g. Edelson et al. 2019). This, together with the fact that the X-rays are more rapidly variable than the UV (see Section 3.3.2 on the multi-wavelength

PSDs) is the best evidence that the weeks to months timescale variability observed in the UV/optical originates from reprocessing of X-rays from corona. The disk does produce its own variability due to turbulence (see Section 3.3.4 on propagating fluctuations), but at the radii where the optical and UV peak, this variability is much slower (hundreds of years), and is not typically observed (though see Hernández Santisteban et al. 2020 and Yao et al. 2023 for detection of propagating fluctuation lags in Fairall 9, seen only by removing more rapid variability associated with reverberation).

While the corona-disk reverberation picture generally holds, there are caveats: We uniformly observe that the amplitude of these lags are several times longer than expected for a standard Shakura-Sunyaev thin disk (Edelson et al. 2019). This, together with the fact that the U band (containing the Balmer jump from the BLR) shows an excess lag inconsistent with just reverberation from the disk, has led to the conclusion that there is some contribution from the BLR in these disk lags (although the exact contribution of the BLR lag is still debated; Kammoun et al. 2019, Chelouche et al. 2019). One solution to the "too-long-lag" problem is to have a better treatment of the ionizing source. If one accounts for the geometry and energetics of the variable corona, and the fact that some of the light that irradiates the disk is reprocessed as fluorescence lines (what we often refer to as "X-ray reflection"), while some is re-emitted in the optical/UV, it can nicely explain the observed lag amplitude (Kammoun et al. 2019), PSD shapes and normalizations (Panagiotou et al. 2022b), SED (Kammoun et al. 2024b), and the amount of correlation between X-ray and UVOIR light curves (Panagiotou et al. 2022a). X-ray reverberation lags also provide independent constraints on the geometry and energetics of the corona, and so future work modeling both X-ray and UVOIR disk lags will be an important step.

# 3.6. The ubiquitous soft excess, and its debated origin

In a large fraction of Seyfert 1 AGN (at least  $\sim 50\%$ , e.g.; Boissay et al. 2016) a soft excess component is observed peaking below  $\sim 1-2\,\mathrm{keV}$  (Figure 9, left). Its origin has been discussed over the years. Initially this soft excess was believed to be the hard tail of UV blackbody emission from the accretion disk (Singh et al. 1985, Arnaud et al. 1985, Pounds et al. 1986, Magorrian et al. 1998, Leighly 1999); however, this explanation was ruled out given that systems with very different accretion rates and/or masses could be characterized by the same blackbody temperature, which is not expected for an accretion disk (Gierliński & Done 2004, Porquet et al. 2004, Piconcelli et al. 2005, Miniutti et al. 2009, Bianchi et al. 2009).

The current models that have gained the most traction in the last years are: (1) Comptonization of UV photons in a "warm" corona, and (2) ionized-blurred reflection. In the first case, the disk photons are Comptonized by an extended warm corona above the disk, which is optically thicker ( $\tau \sim 10-40$ ) and cooler ( $T \sim 10^6$  K) than the corona responsible for the primary X-ray emission (Czerny & Elvis 1987, Middleton et al. 2009, Jin et al. 2009, Done et al. 2012b). In the second case, the emission lines produced by the disk are relativistically blurred due to the proximity to the black hole (see Sec. 3.4. Also see Crummy et al. 2006, Fabian et al. 2009, García & Kallman 2010, Walton et al. 2013, Vasudevan et al. 2014).

**3.6.1. The Warm Corona Model for the soft excess..** For many sources, the performance of these two models in describing the observed data is very similar, although often the warm corona leads to modest improvement in fit statistics (e.g.; Waddell et al. 2023). This is not

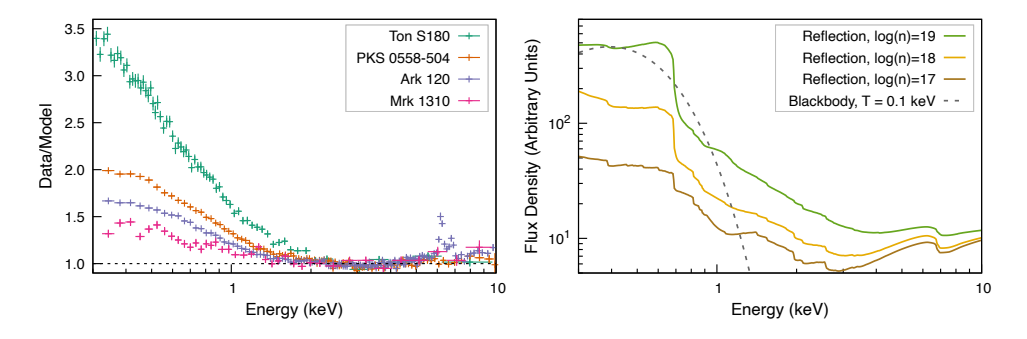


Figure 9

Left: XMM-Newton observations of four representative AGN displaying different amounts of soft-excess emission at low energies, shown as a ratio of the data to a power-law continuum model. Right: Reflection spectra calculated with the relxillCp model for different gas densities, compared to a canonical  $T=0.1\,\mathrm{keV}$  blackbody component typically used as a phenomenological description of the soft excess. XMM-Newton data courtesy of Elias Kammoun (Caltech).

surprising, given that in this picture the soft-excess is modeled with a thermal Comptonization model, which is independent of any of the other model components, particularly of the X-ray coronal emission. Thus, the model has complete freedom to adjust the spectral components independently, acting mostly as a phenomenological description. The thermal Comptonization models often used do not include any source of opacity other than electron scattering by design. On the other hand, models produced with full collisional excitation or photoionization equilibrium predict very strong absorption features in the spectra, which are not observed (García et al. 2019). Recent calculations performed with the TITAN/NOAR code by Petrucci et al. (2020) including an additional source of (mechanical) heating predict featureless spectra. This additional heating presumably raises the gas ionization and diminishes atomic opacities. While this model has been successfully applied to a sample of AGN (Palit et al. 2024), it is unclear how a plasma sufficiently ionized such that no atomic features are imprinted in the spectra, can at the same time produce a continuum with a relatively low temperature. More importantly, the physical origin of this mechanical heating is not specified.

3.6.2. The Relativistic Reflection Model for the soft excess. On the other hand, the reprocessed radiation emergent from the disk—the reflection spectrum—also predicts excess soft-energy flux in the form of a forest of fluorescent emission lines from low-charge elements, or in the form of a bremsstrahlung continuum produced by free-free emission. The latter is significantly enhanced when the gas density in the disk is high (≥ 10<sup>18</sup> cm<sup>-3</sup>; García et al. 2016), which are expected densities for accretion disks around black holes (Shakura & Sunyaev 1973). In fact, high-density reflection models have been used to describe the soft excess in several AGN (e.g.; Jiang et al. 2018b, Mallick et al. 2018, García et al. 2019, Jiang et al. 2019b), and also provide a self consistent explanation for the short soft lags discussed in Sec. 3.5.1). Despite these successes, in several cases the model parameters are pushed to extremes, such as very high densities (so the soft X-ray flux is enhanced), and/or very high spins (so the spectral features are relativistically blurred). While these extreme

parameters do not strictly violate any physical arguments, it could indicate a possible bias in the spin measurements of sources with strong soft excess, particularly in cases where only soft-energy data is included in the analysis (Sec. 3.4). The newest generation of reflection models include high-density plasma effects in the atomic parameters that had been previously neglected (Ding et al. 2024), and show significant departures from standard models in the high-density regime. Further testing of these models on observational data hope to validate the role of reprocessed emission in explaining the soft excess.

3.6.3. Observational Challenges. In general, any model that aims to explain the soft excess must address the surprising lack of correlation between its peak energy and the black hole mass or accretion rate, clearly demonstrated observationally by Bianchi et al. (2009) (see their Fig. 9), while also predicting different possible strengths for the flux in the soft band. Figure 9 shows a comparison of four AGN with different strengths of the soft excess. Given the limited soft-energy band, it is not possible to distinguish if the strength of the soft excess is lower, or if its peak energy is out of the bandpass. Reflection models calculated at high densities produce enough flux below  $\sim 1\,\mathrm{keV}$  capable of mimicking this trend, which would explain the lack of correlation of the peak emission with the black hole parameters. However, the disk density is in fact a function of both mass and accretion rate, and thus there should exist a correlation between black hole mass and/or accretion rate and the strength of the soft excess. Future studies should test the presence of such a correlation.

The assumptions made about the origin of the soft excess directly affect our interpretation of the broadband X-ray spectra from AGN, particularly if related or not to the reprocessed disk emission. The answer to this question can have serious implications on the black hole spin estimates for a large fraction of sources, and consequently in constraining the spin distribution of SMBHs in the local universe (Sec. 3.4). Thus, understanding the origin of the soft excess remains as a relevant issue in AGN physics to be addressed.

# 3.7. Narrow Emission Iron lines: A Probe of the BLR and Dusty Torus

Any cold, dense gas around the black hole will fluoresce as it is irradiated by the X-ray corona. So far, we have focused on the corona irradiation of the accretion disk, where fluorescence lines produced at  $\sim 10~R_g$  are broadened to several keV. But beyond fluorescence from the inner disk, there are also clear signatures of narrow (< 100 eV; < 10,000 km/s FWHM) fluorescence lines from larger scales (Mushotzky et al. 1978) that are seemingly ubiquitous in AGN (Nandra 2006). These fluorescence lines were originally unresolved in X-ray spectra, making it difficult to estimate the distance to the emitting region, but the dusty torus at  $\sim 1$  pc was the presumed emitter, as it was posited to cover  $\sim 50\%$  of the central source (leading to the 50–50 dichotomy of Type 1 and Type 2 AGN; Antonucci 1993; see the review by Hickox & Alexander 2018b).

The launch of Chandra/HETG (Canizares et al. 2000), with  $\sim 30$  eV energy resolution in the Fe K band (several times better than typical CCD spectra), revealed that some of these narrow Fe K lines in fact had line widths of several 1000 km/s (Yaqoob et al. 2001, Costantini et al. 2007, Miller et al. 2018), more suggestive of velocities associated with the optical BLR or outer disk. These spectroscopic measurements are corroborated by narrow Fe K reverberation measurements, where one measures a time lag between the X-ray continuum and the narrow Fe K fluorescence line that is on the order of several days (Ponti et al. 2013, Zoghbi et al. 2019), consistent with the reverberation time delays in optical H $\beta$ 

reverberation lags (Noda et al. 2023). In general, it is understood that at least some of the emission line flux originates from size scales that are well within the dust-sublimation radius of the torus (Shu et al. 2010, Gandhi et al. 2015 for earlier works), though the exact geometry, inclination-dependence and how these complex structures change between different systems is still not well understood (Andonie et al. 2022).

3.7.1. Narrow lines in the XRISM Era. Now with the 2023 launch of XRISM (Tashiro et al. 2018), observations of resolved Fe K lines, which had been challenging and resource intensive for Chandra, are now easy and straightforward. XRISM/Resolve has an energy resolution of  $\Delta E = 4.5$  eV across the 1.6 - 17.4 keV bandpass, providing a resolving power of  $R = E/\Delta E = 1420$  or  $\Delta v = 200$  km/s FWHM at the Fe K line ( $\sim 6.4$  keV). Indeed, the first results for an AGN published by the XRISM Collaboration shows that NGC 4151 (the brightest AGN in the sky) has a very complex iron line profile (XRISM Collaboration 2024 and see Fig. 10). Assuming it fully originates from the blend of Fe  $K\alpha_1$  and Fe  $K\alpha_2$ at restframe energies of 6.404 keV and 6.391 keV, it requires broadening at three different velocities that can be associated to distances assuming Keplerian motion. This suggests emission from the torus ( $\sim 10^4 R_q$ ), the BLR ( $\sim 10^3 R_q$ ), and the accretion disk ( $\sim 10^2 R_q$ ). This analysis was limited to the  $6-6.6\,\mathrm{keV}$  range, and thus was not sensitive to even broader lines that could originate from the inner disk. What is key about XRISM, is that beyond estimating line widths via simple Gaussian modeling, we can now definitively measure the profile of the emission lines (e.g.; Miller et al. 2018), including (relativistic) Doppler shifts, which will allow for high-fidelity estimates of the inclination and geometry of the emitting region. In addition to more sophisticated modeling of the dynamics of the gas, we similarly require a more detailed treatment of the atomic physics (e.g.; Kallman et al. 2021, Mendoza et al. 2021), including proper treatment of the ionization state of the gas (e.g.; with codes such as XILLVER; García et al. 2013). XRISM measurements (especially together with optical spectroscopic and reverberation measurements, and interferometric observations with the GRAVITY VLTI that spatially resolve the BLR) offer a promising future to selfconsistently map gas flows from parsec scales down to the inner accretion disk.

# 3.8. AGN Outflows: The search for AGN Feedback in action

3.8.1. X-ray Absorber: From slow outflows to ultrafast disk winds. The X-ray spectrum also imparts information about optically-thin gas around the nucleus. The material is assumed to be distributed equatorially, and when intercepts our line of sight, we see its signatures in absorption. Typically this material detected via absorption is ionized (either photoionized from the central source or collisionally ionized), and often is observed to be outflowing at hundreds of km/s, and sometimes up to  $0.1-0.4\,c$ .

AGN outflows are essential in understanding the role of SMBHs in galaxy evolution, as they can induce or suppress star formation, expel gas from the host galaxy, or halt accretion (Silk & Rees 1998, Fabian et al. 2012). Theoretical models infer that outflows with kinetic luminosities ranging from 0.5–5% Eddington luminosity of the black hole are necessary to have a substantial impact on galaxy evolution (Di Matteo et al. 2005, Hopkins & Quataert 2010), and thus there is much interest to understand the energetics and launching mechanisms of these outflows. However, to date, observational evidence of outflows capable of generating such feedback has been elusive.

AGN outflows manifest in several ways and on many scales: from the narrow-line re-

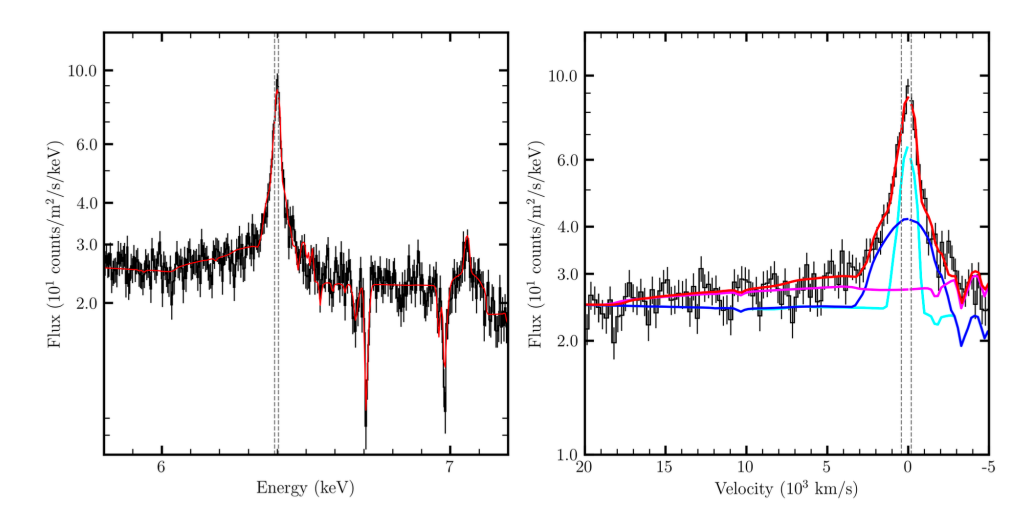


Figure 10

Left: The XRISM spectrum of NGC 4151, zoomed in to the iron line region. The narrow emission line is resolved, and consists of three components, with velocities right consistent with the Keplerian velocity at the torus (cyan), inner broad line region (blue) and outer accretion disk (red). See Section 3.7 for details. In addition to the emission line, there are absorption lines from Fe XXVI transitions, blueshifted by a few hundred km/s (Section 3.8 for details). Figure from XRISM Collaboration (2024).

#### Warm Absorber:

Slow outflows of < 1000 km/s that typically originate at ~parsec scales.

#### **Ultrafast Outflows:**

Powerful, relativistic outflows of > 0.1c launched from the inner accretion disk.

gion (NLR) and outer BLR, known in the literature as "warm absorbers" with low velocities (< 1000 km/s; Reynolds & Fabian 1995, Behar et al. 2001); to outflows at the inner BLR/outer accretion disk, sometimes referred to as "obscurers" (1000 - 5000 km/s; e.g.; Mehdipour et al. 2016); to fast outflows launched at the inner accretion disk, called "Ultrafast Outflows" (UFOs; e.g.; Pounds et al. 2003) that can reach velocities of 0.1-0.4 c. The literature is vast, and the nomenclature for different "types" of outflows can be jarring for the uninitiated, but it is possible that the outflows that we observe are all part of the same streamline, where UFOs launched from the inner regions eventually manifest as the slower, less ionized warm absorbers at larger scales (Tombesi et al. 2013). It is even posited that the optical BLR is a "failed" accretion disk wind, where the outflow velocity did not exceed the escape velocity, and falls back towards the disk (Czerny & Hryniewicz 2011). Understanding where these outflows are launched, how powerful they are, and if/how they couple to outflows at large scales (even out to galaxy-scale flows seen in sub-mm, IR and optical) is the subject of much important ongoing work. We invite interested readers to see the recent reviews by Gandhi et al. 2022 and Gallo et al. 2023 for more details.

**3.8.2. Future prospects for AGN Outflows.** Ultimately, we want to understand how the growth of the central supermassive black hole via accretion leads to large scale coupling to the growth of the galaxy, and to answer this question, not only do we need to understand which of these outflows are energetic enough to be responsible for large-scale feedback, but also how the accretion of matter on to the black hole launches these outflows. This is where spectroscopic time-domain campaigns are particularly powerful. If we can monitor

the stochastic nature of the ionizing source, we can use the evolution of the spectra and the reverberation lags to understand the accretion disk and corona geometry, and subsequently, we can follow how the outflows change in response to these variations in the central engine. We can track how long it takes for the ionization state of the gas to respond to changes in the ionizing luminosity (as the recombination timescale of the outflow is very sensitive to the outflow density, a major uncertainty in determining the launching radius; Rogantini et al. 2022, Sadaula et al. 2023). By tracking the outflow evolution in time, we can test if the outflow velocity is set by the amount of continuum flux (as expected from radiation driven winds), or if more complex physics (i.e. magnetic fields) are at play. There have been attempts at coupling long-term multi-wavelength reverberation mapping campaigns with spectroscopic studies of the outflows (e.g. De Rosa et al. 2015, Kara et al. 2021). With improved time domain surveys (like Rubin in the optical and ULTRASAT in the UV), coupled with spectroscopic monitoring in the UV (with e.g. UVEX) and the X-ray (with, e.g. XRISM), we can probe the causal connection between accretion and ejection to answer some of the fundamental questions about the role of black holes in galaxy evolution.

# 4. EXTREME VARIABILITY IN SUPERMASSIVE BLACK HOLES

As reviewed in the last section, AGN are extremely variable in X-rays. Because of their stochastic nature, we expect that each time we point our telescopes, we will see a different flux and a different variability pattern. But sometimes, this variability is beyond random fluctuations drawn from the same underlying physical process, and instead indicates a state transition that could drastically change the accretion rate of the AGN. With cadenced surveys (e.g. starting in the 1990s with the ROSAT all-sky survey with a 6-month cadence, and to today, with optical time-domain surveys that scan the sky every few days), we are discovering more such extreme transients that indicate transformations in their accretion flow properties, perhaps due to the presence of stars in the nuclear regions, or even other black holes (both supermassive and stellar mass).

In this Section, we discuss some of the known and theorized nuclear transients, and what they can tell us about how black holes grow and affect their environments. We review what sets them apart from the standard AGN described in the previous section (see Fig. 11 for a comparison). Finally, we describe what is possible with higher signal-to-noise X-ray observations.

# 4.1. Tidal Disruption Events

A Tidal Disruption Event (TDE) occurs when a star approaches too closely to a SMBH to the point where the gravitational tidal forces exceed the self-gravity holding the star together. This process tears the star apart into a stream of stellar debris, some of which is gravitationally bound to the black hole, and forms an accretion disk around it. See Gezari (2021) for a much more in-depth review of their multi-wavelength properties. Here, we focus on the X-ray properties of thermal TDEs (i.e. non-jetted), what they can teach us about accretion disk/corona physics, and on a new class of repeating TDEs that share some commonalities with X-ray Quasi-Periodic Eruptions (QPEs; Section 4.3).

**4.1.1. TDEs in X-rays.** The first TDE discoveries were made in the 1990s with the *ROSAT* X-ray observatory (Bade et al. 1996, Komossa 2015a). More recently, its successor,

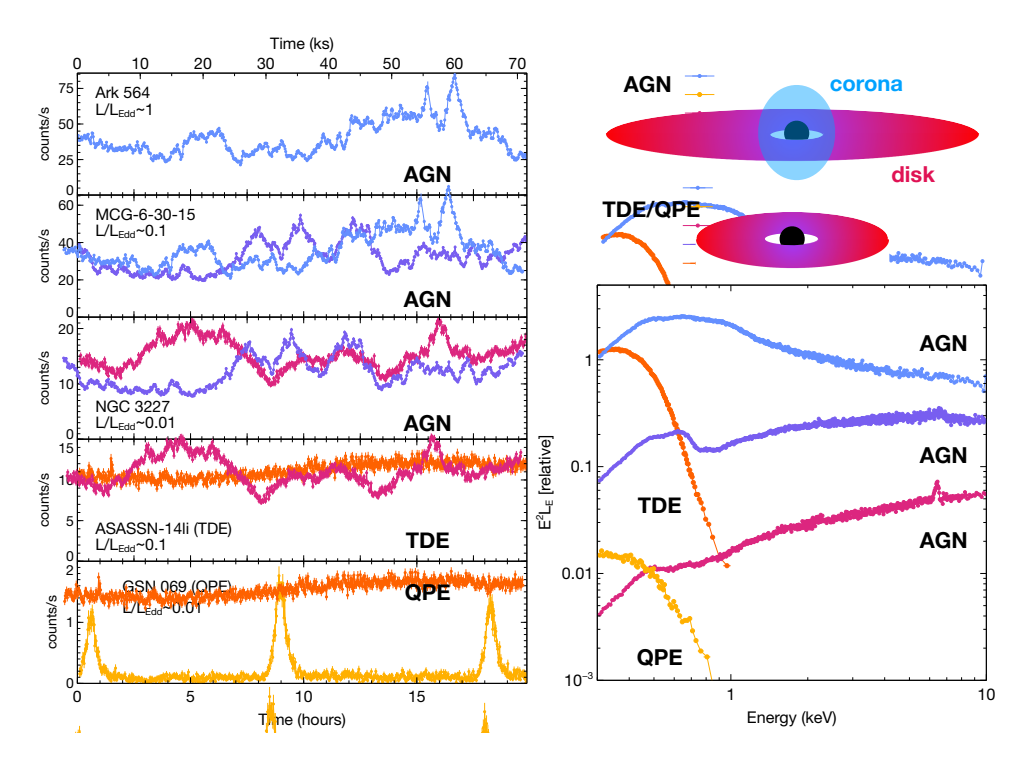


Figure 11

A comparison of the X-ray variability and spectral properties of five  $10^6 M_{\odot}$  accreting SMBHs, at different accretion rates. Left: The top three light curves demonstrate the stochastic nature of AGN light curves at  $L/L_{Edd} \sim 1$ , 0.1 and 0.01. The bottom two light curves are TDE candidates that do not follow the same variability patterns. In particular, the TDE candidate GSN 069 shows strong QPEs every  $\sim 9$  hours. Right: The corresponding spectra for each of these source classes, scaled by their relevant luminosities. All standard AGN show hard X-ray components > 2 keV. The TDE and QPE sources show no hard X-rays above  $\sim 1$  keV, which is largely representative of so-called "thermal" TDEs (Sec. 4.1) and QPEs (Sec. 4.3).

eROSITA, has discovered many more, with tens of confirmed X-ray selected TDEs (Sazonov et al. 2021), and several hundred candidates (Grotova et al. 2025). These events are identified as sources with no prior AGN activity (in X-ray or optical) that show sudden, significant X-ray brightening. The X-rays typically peak at  $L_x > 10^{43}$  erg/s on timescales of < 6 months (the survey cadence) and decay over years, following roughly a  $t^{-5/3}$  power-law. Despite no selection based on spectral shape, these transients consistently exhibit unusually soft, thermal X-ray spectra, matching the predictions of Rees (1988) that TDEs would emit soft X-rays from a  $\sim 10^6$  K accretion disk formed by the circularization of stellar debris.

In the past decade, most TDEs have been discovered in optical time-domain surveys, like ASAS-SN and the Zwicky Transient Facility. Their optical SEDs reveal photosphere temperatures of  $\sim 10^4$  K, much cooler than a newly formed disk around a  $\sim 10^6~M_{\odot}$  black hole (Yao et al. 2023). The origin of the optical emission remains debated, with two leading interpretations: (1) X-rays from the disk are absorbed and reprocessed to longer wavelengths (Roth et al. 2016) by an envelope of unbound debris (Metzger & Stone 2016)

or an optically thick disk wind (Dai et al. 2018), or (2) colliding debris streams produce shocks at large radii (Piran et al. 2015).

Initially, optically-selected TDEs were thought to rarely show X-ray emission, but extended X-ray campaigns have revealed that some TDEs only become X-ray bright hundreds of days after the optical peak (Gezari et al. 2017). In fact, in a systematic study, Guolo et al. (2024a) found that ~ 40% of optically selected TDEs show X-rays at some point, with most exhibiting delayed X-ray rises 100–200 days post-peak. This delay was initially interpreted as evidence for a late-forming accretion disk, supporting the debris-stream collision model for the optical emission (Gezari et al. 2017). However, even if the disk forms promptly, X-rays may only emerge once the reprocessing layer becomes transparent as the accretion rate declines (Thomsen et al. 2022). Regardless of debates on the emission mechanism in the first weeks to months, it is generally agreed that as the fallback rate decreases (over several months to years), the accretion rate on to the black hole will also decrease. This can manifest as a viscously spreading disk that persists much longer than expected from theoretical fallback rate extrapolations (van Velzen et al. 2019, Mummery & Balbus 2020).

**4.1.2.** Where is the X-ray corona in TDEs?. Notably, while hard X-rays (> 2 keV) are a nearly ubiquitous feature of accreting AGN, TDEs, which achieve AGN-like luminosities, typically do not exhibit hard X-ray coronae (Komossa 2015b). This suggests that, similar to black hole X-ray binaries, the accretion rate alone does not determine the production of a corona. Possibly, a critical magnetic flux is required to build up as matter inflows through the disk to eventually trigger the formation of a corona (Begelman & Armitage 2014). As the observed rates of TDEs have increased, and with it extensive X-ray follow-up observations with NICER, Swift/XRT, XMM-Newton, and Chandra, we have been able to monitor these events for years after their peak outbursts (e.g. Jonker et al. 2020). These observations have led to the detection of the late-time formation of X-ray coronae in some TDEs (Kara et al. 2018, Jonker et al. 2020, Guolo et al. 2024a). Moreover, in a few sources with well-monitored X-rays for several weeks to years post-peak, there have been observed "state transitions" where the source changes from disk-dominated to corona-dominated and sometimes back again (Wevers et al. 2021, Yao et al. 2022). Some authors have speculated that these share some properties with the regular state transitions in black hole low-mass XRBs, but as of yet, there is no clear one-to-one mapping of TDE spectral evolution to the "Q-diagrams" of low-mass XRBs. Of course, it is important to remember that accounting for the differences in mass, a typical X-ray binary state transition lasting a few days is the equivalent of thousands of years for a supermassive black hole that is  $10^5$ times more massive. Additional theoretical work is required to reconcile these disparate timescales if indeed they are manifestations of the same underlying physics.

Thanks to this common lack of a corona in TDEs, Mummery & Turner (2024) point out that TDEs may be the most ideal astrophysical systems for probing intrinsic small-scale disk turbulence because we have a clear view of the Wien tail from the innermost radii, whereas the Wien tail in typical AGN is either in the hidden EUV part of the SED (Section 3.1.1) or is "contaminated" by the hard X-ray corona (Section 3.1.2). Therefore, future studies of detailed follow-up of the X-ray variability across a range of TDEs with different viewing angles and accretion rates (and disk scale heights) will probe the disk structure and dynamics, and perhaps also probe how and when magnetic flux can accumulate to produce a corona. As such, while there are clear differences in how AGN and TDEs are fed, these new discoveries of TDEs as short-lived accretion episodes may help us understand more

Q-diagram: X-ray intensity vs. hardness ratio of outbursting XRBs, typically tracing a "q" shape that indicates hysteresis across accretion states.

#### 4.1.3. New discovery space: IMBHs, Recoiling SMBHs, TDE in AGN & Repeating TDEs.

To date, we know of roughly 150 confirmed TDEs (Gezari 2021, Sazonov et al. 2021, Masterson et al. 2024). With this large and growing sample, we have begun to identify characteristics for determining bona fide TDEs beyond simply discovering nuclear flares with a power-law decline in previously quiescent galaxies. This allows us to extend our searches of TDEs, opening new discovery spaces. For instance, because we know that many TDEs have super-soft X-ray spectra, strong high-ionization lines like He II, or Bowen fluorescence lines (e.g. van Velzen et al. 2019), we can begin to loosen requirements that bona fide TDEs exist in the nuclei of galaxies. This could allow for the discovery of TDEs from Intermediate Mass Black Holes (IMBHs; Maksym et al. 2014) or recoiling SMBHs (Ricarte et al. 2021). We can also loosen the requirement that the pre-existing galactic nucleus be quiescent. Given that processes like galaxy mergers can drive both stars and gas towards the central black hole, we should expect that some TDEs will occur in AGN. This has led to the discovery of several TDE-in-AGN candidates (Blanchard et al. 2017, Ricci et al. 2020), some of which have been labeled as "Changing-Look AGN" (see next Section 4.2).

We can also begin to loosen requirements on the light curve behavior to search for repeated activity from a TDE. Such repeated TDEs are expected theoretically: only stars where the pericenter of its orbit is smaller than the tidal disruption radius will be destroyed, but many stars will have slightly larger pericenter distances, and in these systems the outer envelope of the star can get stripped off, causing a partial TDE (pTDE) (Guillochon & Ramirez-Ruiz 2013, Coughlin & Nixon 2019). The rate of pTDEs could be orders of magnitude higher than that of complete TDEs (Stone & Metzger 2016), and have been theorized to contribute significantly to the growth of SMBHs (Bortolas et al. 2023). If the stellar remnant follows an elliptical orbit after a pTDE, it may be disrupted again after returning to pericenter, leading to repeating partial TDEs.

Observationally, the prototype object in this emerging source class of repeating pTDEs is ASASSN-14ko (Payne et al. 2021) that shows repeated optical and X-ray flares every 114 days. Several other repeating events have recently been observed over timescales of months to years (Wevers et al. 2023, Malyali et al. 2023, Somalwar et al. 2023, Evans et al. 2023). It remains unclear how a partially disrupted star dissipates enough kinetic energy to be bound to the black hole with a period as short as  $\sim 100$  days. This has sparked a flurry of new theoretical ideas, including the break-up of stellar binaries (Cufari et al. 2022, Lu & Quataert 2023a) or the presence of SMBH binaries (Melchor et al. 2024). Whatever their origin, these new repeating and pTDEs offer a new way to probe the types of stars that are disrupted, and provide a broader understanding of the dynamics of stars in galactic nuclei.

#### 4.2. Changing-Look AGN

Concurrent with the discovery of TDEs was the discovery of other extreme variability phenomena occurring in the centers of active galaxies: so-called "Changing-Look" (CLAGN)<sup>7</sup>

<sup>&</sup>lt;sup>7</sup>The term CLAGN can refer both to AGN with variability due to accretion-rate changes (sometimes specified as "Changing-State" AGN), and those where the variability is due to obscuration along the line-of-sight (so-called "Changing-Obscuration" AGN). Here we use the term CLAGN to discuss only those that are definitively changing in accretion rate. See recent reviews by Ricci & Trakhtenbrot 2023, Komossa et al. 2020 for more details and perspectives, and reviews of changing-

Type 1 AGN				
TDE	At Peak $L_{\rm X} \sim 10^{41-43} {\rm \ erg/s}$	Late Time $L_{\rm Y} \sim 10^{41-43} {\rm erg/s}$	Long-term Trend Varied phenomenology:	Rapid Variability Varied phenomenology:
-27/15	Thermal disk ( $kT \sim 0.05 \text{ keV}$ ) No hard X-rays	Sometimes late-time hard X-rays	50%: Fast rise, slow decay 50%: Late X-ray rise	Generally not as variable when corona not present
QPE	Quiescence	Flares	Long-term Trend	Rapid Variability
	$L_{\rm X} \sim 10^{40-41}~{\rm erg/s}$ Thermal disk ( $kT \sim 0.05~{\rm keV}$ ) No hard X-rays	$L_{\rm X} \sim 10^{42-43} \ {\rm erg/s}$ Soft flares ( $kT \sim 0.1 \ {\rm keV}$ ) No hard X-rays	Varied phenomenology: 50%: Similar to TDEs. 50%: Little X-ray evolution detected	Steady quiescent emission Rapid quasi-periodic flares on hours-days timescale
	At Peak	Late Time	Long-term Trend	Rapid Variability
SMBHB	Predicted Thermal mini-disk emission.	Predicted sharp X-ray drop pre-merger	Predicted sinusoidal variations at orbital period	Predicted stochastic variability
XRB	Hard State	Soft State	Hard State	Soft State
₹,	Strong corona, $\Gamma \sim 1.7$ Weak/no disk, $kT \sim 0.1~{\rm keV}$ broad iron line	Strong disk ( $kT \sim 1~{ m keV}$ ) Weak/no corona Weak/no broad iron line	Stochastic variability X-ray reverberation lags Type C QPOs at 0.1-10 Hz	Little variability No X-ray time lags Weak/no QPOs

Figure 12

Table summarizing some of the key spectral and timing properties of the different source types described in this review article. Accretion is by its very nature stochastic, and so there are exceptions to nearly all of these properties, but we attempt to summarize as a way to gain some traction on the vast phenomenology.

(Matt et al. 2003), where AGN are seen to dramatically change in bolometric luminosity (beyond the stochastic variability discussed in Section 3.3) on timescales of several months to years—faster than the expected viscous timescale at the outer accretion disk (See Eq. 10)<sup>8</sup>.

Whereas the study of TDEs had the benefit of starting from a strong theoretical foundation (one predicted strong, fast flare rising to AGN-like luminosities in *previously quiescent*, low-mass galaxies), many other supermassive black holes exhibited extreme variability that did occur in systems with previous AGN activity, and therefore could not definitively be characterized as TDEs.

The phenomenology of CLAGN is complex and likely indicates that their origin is also varied. They have been posited to be due to stars in the nuclear environments interacting with the AGN disk (McKernan et al. 2022, Chen & Lin 2024), binary supermassive black holes (Wang & Bon 2020), extreme in situ disk instabilities (Raj & Nixon 2021), or due to reprocessing of a highly variable X-ray/EUV source (Lawrence 2018, Noda & Done 2018). As such, they have garnered much attention, but despite knowing of these events for over two decades, this is a field much in its infancy because of the complex and heterogeneous phenomenology. It is likely that in years to come, as larger all-sky and panchromatic observatories come online, this coarse description of extreme AGN variability will splinter into several new and exciting sub-fields.

obscuration events.

<sup>&</sup>lt;sup>8</sup>The viscous timescale at  $\sim 10^3 R_q$  for a  $10^8 M_{\odot}$  AGN is roughly  $t_{\rm visc} \sim 500 \, {\rm years}$ .

4.2.1. Optically-selected CLAGN. Early optical papers defined CLAGN as those that showed the (dis)appearance of the broad emission lines, indicating a transition between Type 1 and Type 2 AGN (MacLeod et al. 2016). The appearance of Type 1 broad lines was accompanied by a significant rise in the blue continuum (indicating a rise in the thermal emission from the accretion disk). The dramatic change in broad emission lines tells us that the unseen far-UV must be changing even more dramatically than the optical continuum, thus confirming their extreme nature (Lawrence 2018). Recent SDSS-V spectroscopic studies suggest that  $\sim 0.4\%$  of AGN may be CLAGN, with this fraction increasing by a few per cent in systems of lower mass (Zeltyn et al. 2024).

In recent years, there has been several efforts to identify CLAGN via optical photometric observations alone. Both photometric and spectroscopic approaches require care, as even stationary red noise processes can lead to one-off high-amplitude flares and do not necessarily indicate a physical change to the system (see e.g. Uttley et al. 2005 for a discussion of seemingly dramatic flares that arise from random realizations of a uniform physical process, in the context of black hole XRBs). These systematic statistical approaches (e.g. López-Navas et al. 2023, Wang et al. 2024b) are important for developing homogeneous samples, and will become even more vital in the *Rubin* era, as our sample sizes increase.

4.2.2. The X-ray properties of CLAGN. The X-ray properties of CLAGN will be an important piece of the puzzle for understanding their nature, as the X-rays probe the accretion flow and magnetic field structure at the smallest scales. As of yet, there is no clear consensus on what happens to the X-rays in optically-selected CLAGN. In many cases, the X-rays track the observed optical variations (e.g. Krumpe et al. 2017), and in other well-known cases the X-rays do not correlate with the optical. Perhaps the best known case of such phenomenon is 1ES 1927-654 (Trakhtenbrot et al. 2019), where the optical increased by a factor of a few, followed by variations up and down in the X-rays by 4 orders of magnitude, including the disappearance and re-building of the hot X-ray corona. Such varied phenomenology in the X-rays is telling us something, and likely indicates that these extreme optical flares do not all have the same origin.

Future optical discoveries should be accompanied by high-cadence X-ray monitoring (e.g. every few days) to characterize and track the often exotic evolution of the accretion flow structure on the smallest scales. Moreover, we need more real-time discoveries of CS-AGN in the X-rays to understand which comes first: is there a restructuring of the X-ray emitting inner accretion flow (where the viscous timescale is short, on the order of days) that—due to reprocessing—drives the optical variability that we observe, or is the CLAGN a much more global phenomenon, affecting the outer accretion disk (in the optical), which propagates inwards, thus later affecting the X-ray emitting region. These kinds of coordinated campaigns, multi-wavelength follow-up are vital for understanding the origin of CS-AGN.

# 4.3. Quasi-Periodic Eruptions

Quasi-Periodic Eruptions (QPEs) are an X-ray phenomenon occurring at the centers of galactic nuclei that have recently taken the astronomical community by storm. Discovered in 2019 (and announced rather epically by Giovanni Miniutti at an X-ray conference in Bologna to the shock of many audience-members, including these authors), there are now more theory papers trying to explain this perplexing phenomena than there are sources that

show QPE behavior! QPEs are dramatic X-ray flashes occurring every few hours in a very regular (though not completely periodic) way. At the time of writing this review article, there are 9 confirmed QPEs (Miniutti et al. 2019, Giustini et al. 2020, Arcodia et al. 2021, 2024b, Nicholl et al. 2024, Hernandez-Garcia et al., in press, Chakraborty et al. 2025) and 2 candidates that show similar properties, but have only shown  $\sim 2$  flares (Chakraborty et al. 2021, Quintin et al. 2023, Bykov et al. 2024).

**4.3.1. QPE observables.** The first QPE was discovered serendipitously, while examining the X-ray light curves of a peculiar nuclear transient, GSN 069 (Miniutti et al. 2019). The other confirmed and candidate QPE sources show similar behavior. They have typical peak luminosities of  $10^{42-43}$  erg/s, and typical recurrence times of several hours to days. They show soft X-ray spectra (with no hard X-ray corona!). In quiescence, they are well modeled by thermal accretion disks with  $kT \sim 50-80$  eV, and during flares, they universally show hotter thermal-like spectra ( $kT \sim 100-250$  eV), with the characteristic temperature hysteresis suggesting an expending emitting region during the flare (Miniutti et al. 2019). Some show very regular flaring (even a beautiful repeating long-short behavior of the flares; e.g. Arcodia et al. 2024a), while others are less regular in their recurrence times (Giustini et al. 2020, Chakraborty et al. 2024). All occur in the nuclei of low-mass galaxies, in systems with masses ranging from  $10^{5.5-6.5}M_{\odot}$ , but as of yet, we do not see clear correlations in the recurrence time or flare duration with the black hole mass.

More than half of the known QPE candidates take place in known TDE or CLAGN, and all (so far) occur several years after the peak luminosity (Miniutti et al. 2019, Chakraborty et al. 2021, Quintin et al. 2023, Nicholl et al. 2024). Moreover, the host galaxies of QPEs and TDEs both show an over-representation in post-starburst galaxies (Wevers et al. 2022). Interestingly. their optical spectra show no broad lines (suggesting there is intrinsically no BLR in these systems), though many do have narrow high-ionization lines, consistent with some past AGN-like activity (Wevers et al. 2022). This is corroborated by recent MUSE studies that reveal that there is an over-representation of extended emission line regions in these systems, suggesting ionization from a previous, short-lived SMBH flare (Wevers et al. 2024).

It is now incontrovertible that some—if not all—QPEs occur in TDEs, but we cannot yet say that they *must* occur in TDEs. In standard AGN, where there are strong coronae that show multi-frequency red noise (Section 3.3), it would be harder to convincingly pick out a  $\sim 1000$  s quasi-periodic flare above the stochastic red noise background, and so physical models that predict QPEs in both TDEs and AGN are not currently ruled out by observations.

**4.3.2.** Models for the origin of QPEs. There are two general flavors of models for the origin of QPEs: accretion disk instabilities or the interaction of an orbiting low-mass object (star or black hole) with the central SMBH.

The disk instabilities models find inspiration in observations of some exotic black hole low-mass X-ray binaries like GRS 1915+105 and IGR J17091-3624, which are known to show highly structured dramatic flaring light curves on a range of timescales from hundreds of seconds down to sub-second (Belloni et al. 2000, Altamirano et al. 2011, Wang et al. 2024a). These have been explained by radiation pressure instabilities that cause a narrow ring in the accretion flow to oscillate between stable and unstable modes of accretion as the ring heats and cools (Sniegowska et al. 2020), or by warped accretion disks that can tear

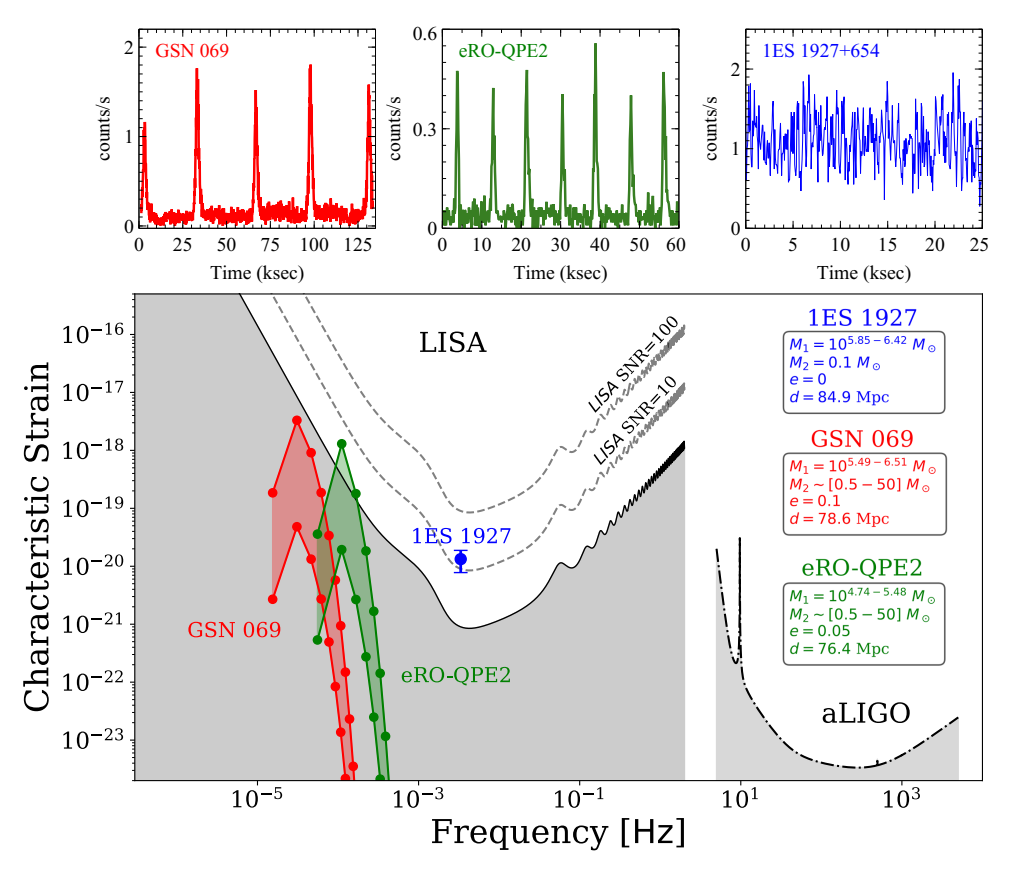


Figure 13

Top: Example light curves of two Quasi Periodic Eruptions, GSN 069 (red) and eRO-QPE2 (green), which show periodic flaring on timescales of hours, and the X-ray light curve of 1ES 1927+654 (blue) that shows a  $\sim$  10-minute period. A leading model for QPEs is that they are due to the interaction of an Extreme Mass Ratio Inspiral with the accretion disk of the supermassive black hole it is orbiting. If the orbiter model is correct, QPEs will be potential LISA gravitational wave sources. Bottom: The LISA sensitivity curve (shaded gray region) highlights the frequency range where LISA can detect signals, with dashed lines indicating signal-to-noise ratios (SNR) of 10 and 100. Overplotted are the predicted gravitational wave signals for GSN 069 (red), eRO-QPE2 (green), and 1ES 1927 (blue) based on the mass, eccentricity, and distance parameters, assuming an EMRI model. The ranges shown for GSN 069 and eRO-QPE2 reflect our uncertainty in the origin of the orbiter, whether it is a  $0.5M_{\odot}$  star or a  $50M_{\odot}$  black hole. The authors thank Joheen Chakraborty (MIT) for producing the LISA characteristic strain plot, and Megan Masterson (MIT) and Riccardo Arcodia (MIT) for the light curves.

and break into discrete rings that accrete at timescales faster than the local viscous time (Raj & Nixon 2021).

More widely explored are the orbiter models, where QPEs have been proposed as due to repeated partial tidal disruption events (King 2022), Roche-lobe overflow of a main-sequence star in a mildly eccentric orbit around the black hole (Lu & Quataert 2023b, Krolik & Linial 2022, Metzger et al. 2022) or stars/black holes (known as Extreme Mass

Ratio Inspirals or EMRIs) colliding with a pre-existing disk, or a disk formed in a TDE (Linial & Metzger 2023, Franchini et al. 2023). The EMRI-disk collision models are particularly adept at explaining the observed long-short pattern observed in some QPEs, as the EMRI (star or compact object) on a mildly eccentric orbit passes twice per orbit through the accretion disk, each time shocking and ejecting material from the disk that expands throughout the flare. In this scenario, the cross section of the EMRI with the disk determines the amplitude of the flare. Linial & Metzger (2023) find the cross section of a star is sufficient, while a compact object would need to be relatively high mass (e.g. a black hole with  $\sim 50-100~M_{\odot}$ ) to have a Bondi radius large enough to explain the observed amplitudes.

EMRI, Extreme
Mass Ratio Inspiral:
Typically refers to a
stellar mass object
orbiting a
supermassive black
hole.

4.3.3. How will we determine the origin of QPEs?. QPEs have the benefit of being regular, almost deterministic time series, that we can predict and model. The EMRI model—at its essence—allows for predictions for when and how long flares occur. Of course, these are not clean EMRI systems, as most numerical relativists have largely focused on, and the presence of an accretion disk (that may be warped or even precessing; Franchini et al. 2023) does significantly complicate the models, but in time, with long enough baselines, we should be able to put models to the test by predicting future flares. Already, multi-year monitoring programs are being used to test period modulations predicted by EMRI models (Chakraborty et al. 2024, Arcodia et al. 2024a, Miniutti et al. 2024).

The incontrovertible proof that QPEs are associated with EMRIs orbiting a SMBH would come from the joint detection of a QPE with a gravitational wave signal from LISA. Arcodia et al. (2024a) estimate that if QPEs are caused by EMRIs, then those with 2-20 hr flare recurrence times (of which there are currently 3 known) would emit GWs in the frequency range of  $10^{-5}$  to  $10^{-4}$  Hz, which is on the lower end of the frequency range where LISA is sensitive (Fig. 13). If the orbiter is a  $40-100M_{\odot}$  black hole, LISA could detect strains of  $10^{-18}$  to  $10^{-17}$  at an SNR of  $\sim 1$  for known QPEs. If the orbiter is a star, the known QPEs would be undetectable. Most recently, we discovered that another similar nuclear transient, 1ES 1927+654, exhibits even higher frequency quasi-periodic flaring that evolve over two years from an 18 min period down to 7 min (Masterson et al. 2025). If this source is also associated with an EMRI, it will emit gravitational waves at mHz frequencies, where LISA is most sensitive, and would be detected at an SNR  $\sim 10$ .

While it remains to be seen whether the currently known QPEs will be LISA sources, they nonetheless inform our understanding of the dynamics of stars in galactic nuclei. Many models proposed for QPEs can also account for longer-period nuclear transients (e.g., Evans et al. 2023, Guolo et al. 2024b, Pasham et al. 2024) and repeating partial TDEs in Section 4.1.3), and these same models predict even closer encounters that would be detectable by LISA (Linial & Metzger 2023, Metzger et al. 2022, Melchor et al. 2024). Given the growing number of QPE sources, repeating pTDEs and in light of recent discoveries of mHz oscillations around supermassive black hole transients (Pasham et al. 2019, Masterson et al. 2025), we consider it a hopeful prospect for future joint X-ray+LISA EMRI detections. This joint detection would allow for unprecedented understanding of accretion disks (as angular momentum losses from gas drag can dominate gravitational wave emission, and are extremely sensitive to the disk structure and surface density), as well as precision cosmology measurements.

## 4.4. Supermassive black hole binary candidates

One of the key predictions of hierarchical structure formation is that supermassive black holes (SMBHs) grow through successive mergers following the coalescence of their host halos. These SMBH mergers emit gravitational waves, detectable by Pulsar Timing Arrays (PTAs) for black holes in the range of  $10^8 M_{\odot}$  to  $10^{10} M_{\odot}$ , and by LISA for those in the range of  $10^5 M_{\odot}$  to  $10^7 M_{\odot}$ . The recent NANOGrav PTA discovery of a potential gravitational wave background from a population of SMBHBs (Agazie et al. 2023) and ESA's approval of the LISA mission for a 2035 launch (Amaro-Seoane et al. 2017) highlight the growing likelihood of such detections. While no definitive sub-parsec SMBHB has been identified to date, ongoing advancements in theoretical predictions of electromagnetic signatures continue to drive observational searches (Bogdanovic et al. 2022).

4.4.1. Theoretical predictions of EM emission from SMBHBs. The gas dynamics around SMBHBs and the subsequent electromagnetic signatures are highly uncertain, but it is likely that LISA and PTA-detectable, merging SMBHBs will have accretion disks, as they result in the interaction of gas-rich galaxies. It is generally agreed that SMBHB systems with large mass ratios exist in a circumbinary disk (Pringle 1991, MacFadyen & Milosavljević 2008), which feeds mini-disks around the two black hole (Ryan & MacFadyen 2017). The circumbinary disk is expected to emit in optical/UV, while mini-discs will produce thermal emission in soft X-rays and a hard X-ray continuum at luminosities close to the Eddington limit (d'Ascoli et al. 2018). It then follows that as the black holes orbit each other, one should observe periodic luminosity fluctuations at the orbital frequency (i.e. at half the gravitational wave frequency). This signature should be strongest in the X-rays, that are dominated by mini-disk emission, and where strong Doppler beaming effects can enhance the variability amplitude (D'Orazio et al. 2016).

Recent theory works have studied the EM signatures within a few days of merger and soon after merger, and while there remains much debate about the exact dynamics, it is generally predicted that there will be dramatic changes to the broadband SED at the time of merger. For instance, as the black holes get close to merger, they will eventually lose contact with the circumbinary disk, thus depleting the gas reservoir to the mini-disks, which may result in a drop of the X-ray emission right before merger (Farris et al. 2015, Dittmann et al. 2023), perhaps by several orders of magnitude (Krauth et al. 2023). Moreover, the anisotropic GW emission at merger will result in sudden mass-loss of the black hole (perhaps by a few per cent; Tichy & Marronetti 2008) and a recoil kick of a few hundred km/s (Baker et al. 2008), which can cause the circumbinary disk to fill in, and rebrightening to a single AGN (e.g. Milosavljević & Phinney 2005).

**4.4.2. The ongoing quest for milli-parsec SMBHBs.** The advent of optical time domain surveys that have been running for > 10 years have motivated several studies to systematically search for SMBHBs with orbital modulations of of a few years, corresponding to milli-pc separations (e.g., Graham et al. 2015, Charisi et al. 2016), though no unambiguous binaries have been found. Section 3.3 provides details for why this is such a tricky detection to make. Even single AGN are highly variable, on a range of timescales from hours to years. If one does not have a long enough baseline, or high enough cadence observations, it can be difficult to distinguish between "normal" stochastic AGN variability and a periodic signal. Vaughan et al. (2016) examine this issue in detail, showing that AGN can easily have spurious "phantom periods" (typically  $\sim 3$  cycles). This happens more commonly in steep

red noise power spectra (i.e.  $\alpha > 2$ ), which happens to be what is observed in high-quality optical PSDs; Mushotzky et al. 2011). Moreover, it is known that the PSD shape varies with black hole mass and luminosity (Arévalo et al. 2023), and therefore it is vital to test against the correct null hypothesis that accounts for the diversity of PSD shapes seen. In short, it is not sufficient to test for periods in optical time domain surveys against a null hypothesis of a Damped Random Walk.

**4.4.3. Future prospects for SMBHB discovery.** Fortunately, time-domain surveys are only getting better. Baselines are getting longer, and the quality of the light curves are improving. As such, with Rubin/LSST we have a better chance to robustly detect periodic light curves, but to truly decipher whether periodic behavior is due to merging black holes (rather than some other accretion disk instability or precession), we need to go beyond, and look for independent indicators that a binary is present. Of course, the joint detection of lowfrequency gravitational waves would make this trivial, but until that day, there is still more we can do with electromagnetic observations. For instance, it would be hard to refute the existence of merging binary supermassive black holes if one also finds a negative period derivative consistent with gravitational wave radiation over many (>10) cycles. As the black holes inspiral, one might expect Doppler shifting of the X-ray emission from the mini-disks. If X-ray coronae form in mini-disks and irradiate the disks, one would expect double peaked iron lines or "rocking" iron lines moving from blue-to-red by  $\sim 10,000 \text{ km/s}$ , at the orbital period. One could also search for reverberation lags from the mini-disks that are shorter than those expected from a single AGN with larger accretion disks (e.g. Liu et al. 2024). Finally, as the black holes approach coalescence, we can look for X-ray dips, indicating the final detachment of the mini-disks from their circumbinary disks (e.g. Dittmann et al. 2023, Krauth et al. 2023). Regardless of the exact observables, the X-rays will be an important wavelength for searching for EM emission from SMBHBs, as these mergers are going to be gas-rich, and so the nucleus will likely be heavily extincted in the UV/optical, but bright in X-rays.

While the predicted LISA rates of binary supermassive black hole mergers is highly uncertain, we hope to observe several in the LISA era. Joint X-ray detections will provide vital information on the gas dynamics that enables merger, but they are also important for key gravitational wave studies as well: Gravitational waves are sensitive to the chirp mass, but as the EM observables are very sensitive to the mass ratio, a joint detection will nail down individual component masses. Moreover, gravitational waves alone have a degeneracy between distance and system inclination. X-ray fluorescence lines from the mini-disks can provide a robust measurement of the inclination (see Section 3.4 for inclination constraints from reflection spectroscopy in single AGN). A joint X-ray and GW detection of any binary SMBH candidate will allow us to break the distance-inclination degeneracy, thus enabling precision cosmology measurements beyond the local distance ladder.

### 5. SUMMARY & OUTLOOK

In the last decade, a suite of X-ray missions, each with their own unique capabilities, has greatly expanded our understanding of the inner accretion flow closest to the event horizon. In short:

• As the first hard X-ray focusing mission, with NuSTAR we have an unprecedented view of the relativistically broadened iron K and Compton hump features, which

- enables robust measurements of black hole spin in stellar mass and supermassive black holes (Section 3.4).
- Long uninterrupted XMM-Newton observations of AGN, and corresponding highthroughput NICER observations of stellar mass black holes, have allowed us to measure the corresponding X-ray reverberation lags from light reflected off the accretion disk, solidifying the relativistic reflection interpretation and probing the geometry of the X-ray corona (Section 3.5.1).
- Swift, with its co-aligned X-ray and UV/optical optics, has enabled simultaneous reverberation mapping of the outer accretion disk, so we can probe the connection between the disk and corona, and how that correlates with energy released via accretion disk winds (Section 3.8).
- Now with the recent launch of *IXPE* in 2021 and *XRISM* in 2023, we have opened new windows into X-ray polarization (Section 3.2) and high-resolution X-ray spectroscopy (Section 3.7), respectively. It is likely that the biggest contributions of these missions are yet to come, as we collect more observations and models are developed to explain them. In fact, *IXPE* is already opening new windows in our understanding of the geometry of the X-ray corona and *XRISM* in our understanding of large-scale gas flows in the BLR and the torus.

We are also living a renaissance in black hole accretion physics thanks to new time domain and multi-messenger facilities that are up-ending what we thought we knew about how supermassive black holes grow via accretion and mergers. We are witnessing previously quiescent black holes suddenly "turn on" due to the tidal disruption of unfortunate stars on close-approach to the black hole (Section 4.1); we regularly discover AGN that accrete material on timescales orders of magnitude faster than we thought theoretically possible (Section 4.2); we are seeing exotic quasi-periodic X-ray flaring in disks around supermassive black hole, that are posited to be due to the impact of a stellar mass object with the accretion disk (Section 4.3), and may lead to joint EM-GW discoveries with LISA. We hope to soon discover other LISA sources, too, with the robust discovery of supermassive black hole binaries at milli-parsec separations (Section 4.4), and regular joint detections of accreting SMBHs with high-energy neutrino events.

X-rays are a vital piece of this new time domain and multi-messenger view of supermassive black holes because they probe the regions closest to the event horizon. For instance,

- Although the origin of the optical emission in TDEs is not yet understood, the soft X-rays unambiguously originate from a small, newly formed accretion disk.
- QPEs are an X-ray-only phenomenon, and to date, have no counterpart at longer wavelengths, which tells us that this phenomenon is also occurring close to the supermassive black hole, perhaps making some of them compelling LISA counterparts.
- Binary supermassive black holes at milli-pc distances are thought to have mini-disks that emit in X-rays, with an optical/UV-emitting circumbinary disk. The strongest amplitude periodicity is predicted in the mini-disks. Furthermore, as these are likely gas-rich mergers, the nucleus could suffer from heavy extinction, but X-rays can penetrate.

Several other recent AGN discoveries not covered in this review would also be transformed by concurrent X-ray detections. For instance, JWST is now discovering distant high-z quasar candidates (z > 6) via rest-frame optical spectra of broad Balmer lines, but

with little to no X-ray emission (Yue et al. 2024, Maiolino et al. 2024). Does the lack of X-ray emission mean they are mis-identified as quasars, or that the SED of these luminous systems is unlike typical Type 1 AGN in the local universe? A sensitive X-ray telescope that meets the horizon of *JWST* is needed. Such a concept, the Advanced X-ray Imaging Satellite (AXIS; Reynolds et al. 2023), is currently undergoing a NASA Phase A study for launch in 2032.

Similarly tantalizing, *IceCUBE* is now detecting astrophysical high-energy neutrinos, some of which tentatively appear co-spatial with the two brightest Seyfert AGN in the X-ray band, NGC 1068 (IceCube Collaboration et al. 2022) and NGC 4151 (Abbasi et al. 2024). Several studies suggest these neutrinos originate in the X-ray corona (e.g., Inoue et al. 2020). High-cadence X-ray monitoring of a large AGN sample, aimed at identifying correlations between coronal luminosity and neutrino flux, could provide definitive evidence for this link.

It is truly an exciting time to study supermassive black holes, and X-rays are an essential piece of the panchromatic view to understand their growth via accretion and mergers. With flagship missions *Athena* and *Lynx* slated to be launched in the late 2030s to 2050s, we require a generation of X-ray missions in the next decade to usher us in to this new era of supermassive black hole accretion and growth.

### **DISCLOSURE STATEMENT**

The authors are not aware of any affiliations, memberships, funding, or financial holdings that might be perceived as affecting the objectivity of this review.

#### **ACKNOWLEDGMENTS**

This review has benefited abundantly from the contributions and inspiring discussions from many of our colleagues. We are particularly thankful to (in alphabetical order): Riccardo Arcodia, Peter Boorman, Joheen Chakraborty, Saavik Ford, Yan-Fei Jiang, Tim Kallman, Elias Kammoun, Megan Masterson, Guglielmo Mastroserio, Barry McKernan, Brian Metzer, Richard Mushotzky, Edward Nathan, Scott Noble, Christos Panagiotou, Joanna Piotrowska, Swati Ravi, Dev Sadaula, Navin Sridhar, Phil Uttley, and Marta Volonteri.

## LITERATURE CITED

Abbasi R, Ackermann M, Adams J, Agarwalla SK, Aguilar JA, et al. 2024. arXiv e-prints: arXiv:2406.07601

Abramowicz MA, Fragile PC. 2013. Living Reviews in Relativity 16(1):1

Agazie G, Anumarlapudi A, Archibald AM, Arzoumanian Z, Baker PT, et al. 2023. ApJ 951(1):L8 Alloin D, Pelat D, Phillips MM, Fosbury RAE, Freeman K. 1986. ApJ 308:23

Altamirano D, Belloni T, Linares M, van der Klis M, Wijnands R, et al. 2011. ApJ 742(2):L17

Amaro-Seoane P, Audley H, Babak S, Baker J, Barausse E, et al. 2017.  $arXiv\ e\text{-}prints$  :arXiv:1702.00786

Andonie C, Bauer FE, Carraro R, Arévalo P, Alexander DM, et al. 2022. A&A 664:A46 Antonucci R. 1993. ARA&A 31:473–521

Arcodia R, Linial I, Miniutti G, Franchini A, Giustini M, et al. 2024a. arXiv e-prints :arXiv:2406.17020

Arcodia R, Liu Z, Merloni A, Malyali A, Rau A, et al. 2024b. A&A 684:A64

Arcodia R, Merloni A, Nandra K, Buchner J, Salvato M, et al. 2021. Nature 592(7856):704-707

Arévalo P, Lira P, Sánchez-Sáez P, Patel P, López-Navas E, et al. 2023. MNRAS 526(4):6078-6087

Arévalo P, Uttley P. 2006. MNRAS  $367(2){:}801{-}814$ 

Armitage PJ. 2022. arXiv e-prints :arXiv:2201.07262

Arnaud KA, Branduardi-Raymont G, Culhane JL, Fabian AC, Hazard C, et al. 1985. MNRAS 217:105–113

Bade N, Komossa S, Dahlem M. 1996. A&A 309:L35-L38

Badnell NR. 2006. ApJS 167(2):334-342

Baker JG, Boggs WD, Centrella J, Kelly BJ, McWilliams ST, et al. 2008. ApJ 682(1):L29

Balbus SA, Hawley JF. 1991. ApJ 376:214

Balbus SA, Hawley JF. 1998. Reviews of Modern Physics 70(1):1-53

Baloković M, Matt G, Harrison FA, Zoghbi A, Ballantyne DR, et al. 2015. ApJ 800(1):62

Bambi C, Brenneman LW, Dauser T, García JA, Grinberg V, et al. 2021. Space Sci. Rev. 217(5):65

Bambic CJ, Quataert E, Kunz MW. 2024. MNRAS 527(2):2895–2918

Bardeen JM. 1970. Nature 226(5240):64-65

Bardeen JM, Press WH, Teukolsky SA. 1972. ApJ 178:347-370

Barr P, Mushotzky RF. 1986. Nature 320:421-423

Begelman MC, Armitage PJ. 2014. ApJ 782(2):L18

Begelman MC, Pringle JE. 2007. MNRAS 375(3):1070-1076

Behar E, Sako M, Kahn SM. 2001. ApJ 563(2):497-504

Behar E, Vogel S, Baldi RD, Smith KL, Mushotzky RF. 2018. MNRAS 478(1):399-406

Belloni T, Klein-Wolt M, Méndez M, van der Klis M, van Paradijs J. 2000. A&A 355:271–290

Beloborodov AM. 2017. ApJ 850(2):141

Bertola E, Vignali C, Lanzuisi G, Dadina M, Cappi M, et al. 2022. A&A 662:A98

Bianchi S, Guainazzi M, Matt G, Fonseca Bonilla N, Ponti G. 2009. A&A 495(2):421-430

Blanchard PK, Nicholl M, Berger E, Guillochon J, Margutti R, et al. 2017. ApJ 843(2):106

Blandford R, Meier D, Readhead A. 2019. ARA&A 57:467-509

Blandford RD, Payne DG. 1981. MNRAS 194:1033–1039

Bogdanovic T, Miller MC, Blecha L. 2022. Living Rev. Rel. 25(1):3

Boissay R, Ricci C, Paltani S. 2016. A&A 588:A70

Bortolas E, Ryu T, Broggi L, Sesana A. 2023. MNRAS 524(2):3026-3038

Bowyer CS, Lampton M, Mack J, de Mendonca F. 1970. ApJ 161:L1

Brenneman LW, Reynolds CS. 2006. ApJ 652:1028–1043

Bykov S, Gilfanov M, Sunyaev R, Medvedev P. 2024.  $arXiv\ e\text{-}prints$ :arXiv:2409.16908

Cackett EM, Bentz MC, Kara E. 2021. iScience 24(6):102557

Cackett EM, Gelbord J, Barth AJ, De Rosa G, Edelson R, et al. 2023. ApJ 958(2):195

Cackett EM, Zoghbi A, Reynolds C, Fabian AC, Kara E, et al. 2014. MNRAS 438(4):2980-2994

Canizares CR, Huenemoerder DP, Davis DS, Dewey D, Flanagan KA, et al. 2000. ApJ 539(1):L41–L44

Chainakun P, Young AJ, Kara E. 2016. MNRAS 460(3):3076-3088

Chakrabarti S, Titarchuk LG. 1995. ApJ 455:623

Chakraborty J, Arcodia R, Kara E, Miniutti G, Giustini M, et al. 2024. ApJ 965(1):12

Chakraborty J, Kara E, Arcodia R, Buchner J, Giustini M, et al. 2025. arXiv e-prints: arXiv:2503.19013

Chakraborty J, Kara E, Masterson M, Giustini M, Miniutti G, Saxton R. 2021. ApJ 921(2):L40

Charisi M, Bartos I, Haiman Z, Price-Whelan AM, Graham MJ, et al. 2016. MNRAS 463(2):2145–2171

Chelouche S, Trache D, Tarchoun AF, Khimeche K. 2019. Journal of Energetic Materials 37(4):387–406

Chen YX, Lin DNC. 2024. ApJ 967(2):88

Comisso L, Sironi L. 2018. Phys. Rev. Lett. 121(25):255101

Connors RMT, García JA, Dauser T, Grinberg V, Steiner JF, et al. 2020. ApJ 892(1):47

Costantini E, Kaastra JS, Arav N, Kriss GA, Steenbrugge KC, et al. 2007. A&A 461(1):121-134

Coughlin ER, Nixon CJ. 2019. ApJ 883(1):L17

Crummy J, Fabian AC, Gallo L, Ross RR. 2006. MNRAS 365:1067-1081

Cufari M, Coughlin ER, Nixon CJ. 2022. ApJ 929(2):L20

Czerny B, Elvis M. 1987. ApJ 321:305-320

Czerny B, Hryniewicz K. 2011. A&A 525:L8

Dai L, McKinney JC, Roth N, Ramirez-Ruiz E, Miller MC. 2018. ApJ 859:L20

d'Ascoli S, Noble SC, Bowen DB, Campanelli M, Krolik JH, Mewes V. 2018. ApJ 865:140

Dauser T, García J, Parker ML, Fabian AC, Wilms J. 2014. MNRAS 444:L100-L104

Dauser T, Garcia J, Wilms J, Böck M, Brenneman LW, et al. 2013. MNRAS 430:1694-1708

Dauser T, García JA, Joyce A, Licklederer S, Connors RMT, et al. 2022. MNRAS 514(3):3965-3983

Dauser T, Wilms J, Reynolds CS, Brenneman LW. 2010. MNRAS 409:1534–1540

Davis SW, Tchekhovskoy A. 2020. ARA&A 58:407-439

De Marco B, Ponti G, Cappi M, Dadina M, Uttley P, et al. 2013. MNRAS 431:2441-2452

De Marco B, Ponti G, Petrucci PO, Clavel M, Corbel S, et al. 2017. MNRAS 471:1475-1487

De Rosa G, Peterson BM, Ely J, Kriss GA, Crenshaw DM, et al. 2015. ApJ 806(1):128

Dent WA. 1965. Science 148(3676):1458-1460

Di Matteo T, Springel V, Hernquist L. 2005. Nature 433(7026):604-607

Ding Y, García JA, Kallman TR, Mendoza C, Bautista M, et al. 2024. arXiv e-prints :arXiv:2409.00253

Dittmann AJ, Ryan G, Miller MC. 2023. ApJ 949(2):L30

Done C, Davis SW, Jin C, Blaes O, Ward M. 2012a. MNRAS 420:1848-1860

Done C, Davis SW, Jin C, Blaes O, Ward M. 2012b. MNRAS 420:1848–1860

Dong J, Mastroserio G, Garcia JA, Ingram A, Nathan E, Connors R. 2023. arXiv e-prints :arXiv:2312.09210

D'Orazio DJ, Haiman Z, Duffell P, MacFadyen A, Farris B. 2016. MNRAS 459:2379-2393

Dovčiak M, Podgorný J, Svoboda J, Steiner JF, Kaaret P, et al. 2024. Galaxies 12(5):54

Duras F, Bongiorno A, Ricci F, Piconcelli E, Shankar F, et al. 2020. A&A 636:A73

Edelson R, Gelbord J, Cackett E, Peterson BM, Horne K, et al. 2019. ApJ 870(2):123

Edelson R, Vaughan S, Malkan M, Kelly BC, Smith KL, et al. 2014. ApJ 795(1):2

Edge DO, Shakeshaft JR, McAdam WB, Baldwin JE, Archer S. 1959. MmRAS 68:37-60

Elías-Chávez M, Longinotti AL, Krongold Y, Rosa-González D, Vignali C, et al. 2024. MNRAS 532(2):1564–1579

Elvis M, Maccacaro T, Wilson AS, Ward MJ, Penston MV, et al. 1978. MNRAS 183:129-157

Evans PA, Nixon CJ, Campana S, Charalampopoulos P, Perley DA, et al. 2023. *Nature Astronomy* 7:1368–1375

Fabian AC, Lohfink A, Belmont R, Malzac J, Coppi P. 2017. MNRAS 467(3):2566-2570

Fabian AC, Lohfink A, Kara E, Parker ML, Vasudevan R, Reynolds CS. 2015. MNRAS 451:4375–4383

Fabian AC, Rees MJ, Stella L, White NE. 1989. MNRAS 238:729-736

Fabian AC, Zoghbi A, Ross RR, Uttley P, Gallo LC, et al. 2009. Nature 459:540-542

Fabian AC, Zoghbi A, Wilkins D, Dwelly T, Uttley P, et al. 2012. MNRAS 419(1):116-123

Farris BD, Duffell P, MacFadyen AI, Haiman Z. 2015. MNRAS 447:L80-L84

Fender RP, Belloni TM, Gallo E. 2004. MNRAS 355:1105-1118

Fragos T, McClintock JE. 2015. ApJ 800(1):17

Franchini A, Bonetti M, Lupi A, Miniutti G, Bortolas E, et al. 2023. A&A 675:A100

Frank J, King A, Raine DJ. 2002. Accretion Power in Astrophysics: Third Edition

Galeev AA, Rosner R, Vaiana GS. 1979. ApJ 229:318–326

Gallo LC, Miller JM, Costantini E. 2023. arXiv e-prints :arXiv:2302.10930

Gandhi P, Hönig SF, Kishimoto M. 2015. ApJ 812(2):113

Gandhi P, Kawamuro T, Díaz Trigo M, Paice JA, Boorman PG, et al. 2022. Nature Astronomy 6:1364–1375

García J, Dauser T, Lohfink A, Kallman TR, Steiner JF, et al. 2014. ApJ 782:76

García J, Dauser T, Reynolds CS, Kallman TR, McClintock JE, et al. 2013. ApJ 768:146

García J, Elhoussieny EE, Bautista MA, Kallman TR. 2013. ApJ 775(1):8

García J, Fabian A, Kallman T, Dauser T, Parker M, et al. 2016. Submitted to MNRAS

García J, Kallman TR. 2010. ApJ 718(2):695-706

García J, Kallman TR. 2010. ApJ 718:695-706

García JA, Fabian AC, Kallman TR, Dauser T, Parker ML, et al. 2016. MNRAS 462(1):751-760

García JA, Kara E, Walton D, Beuchert T, Dauser T, et al. 2019. ApJ 871(1):88

García JA, Sokolova-Lapa E, Dauser T, Madej J, Różańska A, et al. 2020. ApJ 897(1):67

García JA, Stern D, Madsen K, Smith M, Grefenstette B, et al. 2024. Frontiers in Astronomy and Space Sciences 11:1471585

George IM, Fabian AC. 1991. MNRAS 249:352-367

Gezari S. 2021. ARA&A 59:21-58

Gezari S, Cenko SB, Arcavi I. 2017. ApJ 851(2):L47

Ghisellini G, Haardt F, Fabian AC. 1993. MNRAS 263:L9-L12

Ghisellini G, Haardt F, Matt G. 2004. A&A 413:535-545

Giacconi R, Gursky H, Paolini FR, Rossi BB. 1962. Phys. Rev. Lett. 9(11):439-443

Gianolli VE, Kim DE, Bianchi S, Agís-González B, Madejski G, et al. 2023. MNRAS 523(3):4468–4476

Gierliński M, Done C. 2004. MNRAS 347:885-894

Gierliński M, Middleton M, Ward M, Done C. 2008. Nature 455(7211):369-371

Giustini M, Miniutti G, Saxton RD. 2020. A&A 636:L2

Gonzalez AG, Wilkins DR, Gallo LC. 2017. MNRAS 472(2):1932-1945

González-Martín O, Vaughan S. 2012. A&A 544:A80

Graham MJ, Djorgovski SG, Stern D, Drake AJ, Mahabal AA, et al. 2015. MNRAS 453(2):1562–1576

Green AR, McHardy IM, Lehto HJ. 1993. MNRAS 265:664-680

Grotova I, Rau A, Salvato M, Buchner J, Goodwin AJ, et al. 2025. arXiv e-prints :arXiv:2501.04208

Grupe D, Komossa S, Leighly KM, Page KL. 2010. ApJS 187(1):64-106

Guillochon J, Ramirez-Ruiz E. 2013. ApJ 767(1):25

Guolo M, Gezari S, Yao Y, van Velzen S, Hammerstein E, et al. 2024a. ApJ 966(2):160

Guolo M, Pasham DR, Zajaček M, Coughlin ER, Gezari S, et al. 2024b. Nature Astronomy 8:347–358

Gupta S, Sridhar N, Sironi L. 2024. MNRAS 527(3):6065-6075

Haardt F, Maraschi L. 1991. ApJ 380:L51

Haardt F, Maraschi L. 1993. ApJ 413:507

Hagen S, Done C, Edelson R. 2024. MNRAS 530(4):4850-4867

Hawley JF, Gammie CF, Balbus SA. 1995. ApJ 440:742

Hazard C, Mackey MB, Shimmins AJ. 1963. Nature 197(4872):1037-1039

Hernández Santisteban JV, Edelson R, Horne K, Gelbord JM, Barth AJ, et al. 2020. MNRAS 498(4):5399–5416

Hickox RC, Alexander DM. 2018a. ARA&A 56:625-671

Hickox RC, Alexander DM. 2018b. ARA&A 56:625-671

Hinkle JT, Mushotzky R. 2021. MNRAS 506(4):4960-4978

Hogg JD, Reynolds CS. 2016. ApJ 826:40

Homayouni Y, De Rosa G, Plesha R, Kriss GA, Barth AJ, et al. 2023. ApJ 948(2):85

Hopkins PF, Quataert E. 2010. MNRAS 407(3):1529-1564

IceCube Collaboration, Abbasi R, Ackermann M, Adams J, Aguilar JA, et al. 2022. Science 378(6619):538–543

Ingram A, Ewing M, Marinucci A, Tagliacozzo D, Rosario DJ, et al. 2023. MNRAS 525(4):5437–5449
Ingram A, Mastroserio G, Dauser T, Hovenkamp P, van der Klis M, García JA. 2019. MNRAS 488(1):324–347

Inoue Y, Khangulyan D, Doi A. 2020. ApJ 891(2):L33

Ishibashi W, Courvoisier TJL. 2012. A&A 540:L2

Jiang J, Fabian AC, Dauser T, Gallo L, García JA, et al. 2019a. MNRAS 489(3):3436-3455

Jiang J, Parker ML, Fabian AC, Alston WN, Buisson DJK, et al. 2018a. MNRAS 477(3):3711-3726

Jiang J, Parker ML, Fabian AC, Alston WN, Buisson DJK, et al. 2018b. MNRAS 477:3711–3726

Jiang YF, Stone JM, Davis SW. 2019b. ApJ 880(2):67

Jin C, Done C, Ward M, Gierliński M, Mullaney J. 2009. MNRAS 398:L16-L20

Jin C, Ward M, Done C, Gelbord J. 2012. MNRAS 420(3):1825-1847

Jonker PG, Stone NC, Generozov A, van Velzen S, Metzger B. 2020. ApJ 889(2):166

Kallman T, Bautista M, Deprince J, García JA, Mendoza C, et al. 2021. ApJ 908(1):94

Kammoun E, Lohfink AM, Masterson M, Wilkins DR, Zhao X, et al. 2024a. Frontiers in Astronomy and Space Sciences 10:1308056

Kammoun E, Papadakis IE, Dovčiak M, Panagiotou C. 2024b. A&A 686:A69

Kammoun ES, Papadakis IE, Dovčiak M. 2019. ApJ 879(2):L24

Kamraj N, Brightman M, Harrison FA, Stern D, García JA, et al. 2022. ApJ 927(1):42

Kaplan SA. 1949. Zhurnal Eksperimental noi i Teoreticheskoi Fiziki 19:951–952

Kara E, Alston WN, Fabian AC, Cackett EM, Uttley P, et al. 2016. MNRAS 462(1):511-531

Kara E, Dai L, Reynolds CS, Kallman T. 2018. MNRAS 474(3):3593-3598

Kara E, García JA, Lohfink A, Fabian AC, Reynolds CS, et al. 2017. MNRAS 468(3):3489-3498

Kara E, Mehdipour M, Kriss GA, Cackett EM, Arav N, et al. 2021. ApJ 922(2):151

Kara E, Steiner JF, Fabian AC, Cackett EM, Uttley P, et al. 2019. Nature 565(7738):198-201

King A. 2022. MNRAS 515(3):4344-4349

King A, Pounds K. 2015. ARA&A 53:115-154

King AL, Lohfink A, Kara E. 2017. ApJ 835(2):226

Komossa S. 2015a. Journal of High Energy Astrophysics 7:148-157

Komossa S. 2015b. Journal of High Energy Astrophysics 7:148-157

Komossa S, Grupe D, Gallo LC, Poulos P, Blue D, et al. 2020. A&A 643:L7

Kotov O, Churazov E, Gilfanov M. 2001. MNRAS 327:799-807

Krauth LM, Davelaar J, Haiman Z, Westernacher-Schneider JR, Zrake J, MacFadyen A. 2023. MNRAS 526(4):5441-5454

Krawczynski H, Muleri F, Dovčiak M, Veledina A, Rodriguez Cavero N, et al. 2022. Science 378(6620):650–654

Krolik JH, Linial I. 2022. ApJ 941(1):24

Krumpe M, Husemann B, Tremblay GR, Urrutia T, Powell M, et al. 2017. A&A 607:L9

Laor A. 1991. ApJ 376:90-94

Lawrence A. 2018. Nature Astronomy 2:102–103

Lawrence A, Papadakis I. 1993. ApJ 414:L85

Leighly KM. 1999. ApJS 125:317-348

Lewin C, Kara E, Barth AJ, Cackett EM, De Rosa G, et al. 2024. ApJ 974(2):271

Lewin C, Kara E, Wilkins D, Mastroserio G, García JA, et al. 2022. ApJ 939(2):109

Lightman AP, Zdziarski AA. 1987. ApJ 319:643

Linial I, Metzger BD. 2023. ApJ 957(1):34

Liu T, Buchner J, Nandra K, Merloni A, Dwelly T, et al. 2022. A&A 661:A5

Liu T, Edelson R, Hernández Santisteban JV, Kara E, Montano J, et al. 2024. ApJ 964(2):167

López-Navas E, Sánchez-Sáez P, Arévalo P, Bernal S, Graham MJ, et al. 2023. MNRAS 524(1):188–206

Lu W, Quataert E. 2023a. MNRAS 524(4):6247-6266

Lu W, Quataert E. 2023b. MNRAS 524(4):6247-6266

Luminari A, Nicastro F, Krongold Y, Piro L, Thakur AL. 2023. A&A 679:A141

Lusso E, Comastri A, Vignali C, Zamorani G, Brusa M, et al. 2010. A&A 512:A34

Lynden-Bell D. 1969. Nature 223(5207):690-694

Lyubarskii YE. 1997. MNRAS 292:679

MacFadyen AI, Milosavljević M. 2008. ApJ 672:83-93

MacLeod CL, Ross NP, Lawrence A, Goad M, Horne K, et al. 2016. MNRAS 457(1):389-404

Magorrian J, Tremaine S, Richstone D, Bender R, Bower G, et al. 1998. AJ 115:2285–2305

Maiolino R, Scholtz J, Witstok J, Carniani S, D'Eugenio F, et al. 2024. Nature 627(8002):59-63

Maksym WP, Lin D, Irwin JA. 2014. ApJ 792(2):L29

Mallick L, Alston WN, Parker ML, Fabian AC, Pinto C, et al. 2018. MNRAS 479:615-634

Malyali A, Liu Z, Rau A, Grotova I, Merloni A, et al. 2023. MNRAS 520(3):3549-3559

Marconi A, Risaliti G, Gilli R, Hunt LK, Maiolino R, Salvati M. 2004. MNRAS 351(1):169-185

Marin F, Gianolli VE, Ingram A, Kim DE, Marinucci A, et al. 2024. Galaxies 12(4):35

Marinucci A, Muleri F, Dovciak M, Bianchi S, Marin F, et al. 2022. MNRAS 516(4):5907-5913

Markoff S, Nowak MA, Wilms J. 2005. ApJ 635(2):1203-1216

Marshall N, Warwick RS, Pounds KA. 1981. MNRAS 194:987-1002

Martocchia A, Matt G. 1996. MNRAS 282(4):L53-L57

Masterson M, De K, Panagiotou C, Kara E, Arcavi I, et al. 2024. ApJ 961(2):211

Masterson M, Kara E, Panagiotou C, Alston WN, Chakraborty J, et al. 2025.  $arXiv\ e\text{-}prints$  :arXiv:2501.01581

Mastroserio G, De Marco B, Baglio MC, Carotenuto F, Fabiani S, et al. 2024. arXiv e-prints :arXiv:2408.06856

Matt G, Guainazzi M, Maiolino R. 2003. MNRAS 342(2):422-426

Matt G, Perola GC, Piro L. 1991. A&A 247:25

McClintock JE, Narayan R, Steiner JF. 2014. Space Sci. Rev. 183(1-4):295-322

McClintock JE, Remillard RA. 2006. Black hole binaries. Cambridge University Press, London, 157–213

McHardy IM, Koerding E, Knigge C, Uttley P, Fender RP. 2006. Nature 444(7120):730-732

McHardy IM, Lawrence A, Pye JP, Pounds KA. 1981. MNRAS 197:893-919

McKernan B, Ford KES, Cantiello M, Graham M, Jermyn AS, et al. 2022. MNRAS 514(3):4102–4110

Mehdipour M, Kaastra JS, Kriss GA, Cappi M, Petrucci PO, et al. 2016. A&A 588:A139

Melchor D, Mockler B, Naoz S, Rose SC, Ramirez-Ruiz E. 2024. ApJ 960(1):39

Mendoza C, Bautista MA, Deprince J, García JA, Gatuzz E, et al. 2021. Atoms 9(1):12

Merloni A, Fabian AC. 2001. MNRAS 321(3):549-552

Metzger BD, Stone NC. 2016. MNRAS 461(1):948-966

Metzger BD, Stone NC, Gilbaum S. 2022. ApJ 926(1):101

Middleton M, Done C, Ward M, Gierliński M, Schurch N. 2009. MNRAS 394:250-260

Miller JM, Cackett E, Zoghbi A, Barret D, Behar E, et al. 2018. ApJ 865(2):97

Milosavljević M, Phinney ES. 2005. ApJ 622(2):L93-L96

Miniutti G, Fabian AC. 2004. MNRAS 349(4):1435–1448

Miniutti G, Franchini A, Bonetti M, Giustini M, Chakraborty J, et al. 2024.  $arXiv\ e\text{-}prints$  :arXiv:2411.13460

Miniutti G, Ponti G, Greene JE, Ho LC, Fabian AC, Iwasawa K. 2009. MNRAS 394:443-453

Miniutti G, Saxton RD, Giustini M, Alexander KD, Fender RP, et al. 2019. Nature 573(7774):381–384

Miyamoto S, Kitamoto S. 1989. Nature 342(6251):773-774

Mizumoto M, Ebisawa K, Sameshima H. 2014. PASJ 66(6):122

Mosquera AM, Kochanek CS, Chen B, Dai X, Blackburne JA, Chartas G. 2013. ApJ 769(1):53

Mummery A, Balbus SA. 2020. MNRAS 492(4):5655-5674

Mummery A, Ingram A, Davis S, Fabian A. 2024. MNRAS 531(1):366-386

Mummery A, Turner SGD. 2024. MNRAS 530(4):4730-4746

Mushotzky RF, Done C, Pounds KA. 1993. ARA&A 31:717-717

Mushotzky RF, Edelson R, Baumgartner W, Gandhi P. 2011. ApJ 743(1):L12

Mushotzky RF, Serlemitsos PJ, Becker RH, Boldt EA, Holt SS. 1978. ApJ 220:790-797

Nandra K. 2006. MNRAS 368(1):L62-L66

Nättilä J. 2024. Nature Communications 15(1):7026

Nicastro F, Fiore F, Perola GC, Elvis M. 1999. ApJ 512(1):184-196

Nicholl M, Pasham DR, Mummery A, Guolo M, Gendreau K, et al. 2024. Nature 634(8035):804-808

Niedźwiecki A, Życki PT. 2008. MNRAS 386(2):759-780

Noda H, Done C. 2018. MNRAS 480(3):3898-3906

Noda H, Mineta T, Minezaki T, Sameshima H, Kokubo M, et al. 2023. ApJ 943(1):63

Novikov ID, Thorne KS. 1973. *Black holes*. Black holes, by C. DeWitt and B.S. DeWitt. New York: Gordon and Breach, 1973.

Nowak MA, Vaughan BA, Wilms J, Dove JB, Begelman MC. 1999. ApJ 510:874-891

Pacucci F, Narayan R. 2024. ApJ 976(1):96

Palit B, Rozanska A, Petrucci PO, Gronkiewicz D, Barnier S, et al. 2024. arXiv e-prints: arXiv:2406.14378

Panagiotou C, Kara E, Dovčiak M. 2022a. ApJ 941(1):57

Panagiotou C, Papadakis I, Kara E, Kammoun E, Dovčiak M. 2022b. ApJ 935(2):93

Panagiotou C, Walter R. 2020. A&A 640:A31

Papadakis I, Pecháček T, Dovčiak M, Epitropakis A, Emmanoulopoulos D, Karas V. 2016. A&A 588:A13

Papadakis IE, Nandra K, Kazanas D. 2001. ApJ 554:L133-L137

Pasham DR, Remillard RA, Fragile PC, Franchini A, Stone NC, et al. 2019. Science 363(6426):531–534

Pasham DR, Tombesi F, Suková P, Zajaček M, Rakshit S, et al. 2024. Science Advances 10(13):eadj8898

Payne AV, Shappee BJ, Hinkle JT, Vallely PJ, Kochanek CS, et al. 2021. ApJ 910(2):125

Peterson BM, Ferrarese L, Gilbert KM, Kaspi S, Malkan MA, et al. 2004. ApJ 613(2):682-699

Petrecca V, Papadakis IE, Paolillo M, De Cicco D, Bauer FE. 2024. A&A 686:A286

Petrucci PO, Gronkiewicz D, Rozanska A, Belmont R, Bianchi S, et al. 2020. A&A 634:A85

Petrucci PO, Merloni A, Fabian A, Haardt F, Gallo E. 2001. MNRAS 328(2):501-510

Piconcelli E, Jimenez-Bailón E, Guainazzi M, Schartel N, Rodríguez-Pascual PM, Santos-Lleó M. 2005. A&A 432:15–30

Piotrowska JM, García JA, Walton DJ, Beckmann RS, Stern D, et al. 2024. Frontiers in Astronomy and Space Sciences 11:1324796

Piran T, Svirski G, Krolik J, Cheng RM, Shiokawa H. 2015. ApJ 806:164

Ponti G, Cappi M, Costantini E, Bianchi S, Kaastra JS, et al. 2013. A&A 549:A72

Ponti G, Fender RP, Begelman MC, Dunn RJH, Neilsen J, Coriat M. 2012. MNRAS 422:L11-L15

Pooley D, Blackburne JA, Rappaport S, Schechter PL. 2007. ApJ 661(1):19-29

Porquet D, Reeves JN, O'Brien P, Brinkmann W. 2004. A&A 422:85-95

Pounds KA, King AR, Page KL, O'Brien PT. 2003. MNRAS 346(4):1025-1030

Pounds KA, Nandra K, Stewart GC, Leighly K. 1989. MNRAS 240:769-783

Pounds KA, Warwick RS, Culhane JL, de Korte PAJ. 1986. MNRAS 218:685-694

Poutanen J, Svensson R. 1996. ApJ 470:249

Poutanen J, Veledina A, Beloborodov AM. 2023. ApJ 949(1):L10

Pozdnyakov LA, Sobol IM, Syunyaev RA. 1983. Astrophys. Space Phys. Res. 2:189–331

Pringle JE. 1991. MNRAS 248:754-759

Prokhorenko SA, Sazonov SY, Gilfanov MR, Balashev SA, Bikmaev IF, et al. 2024. MNRAS 528(4):5972–5989

Quintin E, Webb NA, Guillot S, Miniutti G, Kammoun ES, et al. 2023. A&A 675:A152

Raj A, Nixon CJ. 2021. ApJ 909(1):82

Rees MJ. 1988. Nature 333(6173):523-528

Reeves JN, Braito V, Porquet D, Lobban AP, Matzeu GA, Nardini E. 2021. MNRAS 500(2):1974–1991

Reynolds CS. 2021. ARA&A 59:117-154

Reynolds CS, Fabian AC. 1995. MNRAS 273:1167-1176

Reynolds CS, Kara EA, Mushotzky RF, Ptak A, Koss MJ, et al. 2023. Overview of the advanced x-ray imaging satellite (AXIS). In UV, X-Ray, and Gamma-Ray Space Instrumentation for Astronomy XXIII, eds. OH Siegmund, K Hoadley, vol. 12678 of Society of Photo-Optical Instrumentation Engineers (SPIE) Conference Series

Ricarte A, Tremmel M, Natarajan P, Quinn T. 2021. ApJ 916(2):L18

Ricci C, Ho LC, Fabian AC, Trakhtenbrot B, Koss MJ, et al. 2018. MNRAS 480(2):1819-1830

Ricci C, Kara E, Loewenstein M, Trakhtenbrot B, Arcavi I, et al. 2020. ApJ 898(1):L1

Ricci C, Trakhtenbrot B. 2023. Nature Astronomy 7:1282-1294

Ricci C, Ueda Y, Paltani S, Ichikawa K, Gandhi P, Awaki H. 2014. MNRAS 441(4):3622-3633

Risaliti G, Harrison FA, Madsen KK, Walton DJ, Boggs SE, et al. 2013. Nature 494:449-451

Rogantini D, Mehdipour M, Kaastra J, Costantini E, Juráňová A, Kara E. 2022. ApJ 940(2):122

Ross RR, Fabian AC. 2005. MNRAS 358(1):211-216

Roth N, Kasen D, Guillochon J, Ramirez-Ruiz E. 2016. ApJ 827(1):3

Ryan G, MacFadyen A. 2017. ApJ 835:199

Rybicki GB, Lightman AP. 1979. Radiative processes in astrophysics

Saade ML, Kaaret P, Liodakis I, Ehlert SR. 2024. arXiv e-prints :arXiv:2408.12746

Sadaula DR, Bautista MA, García JA, Kallman TR. 2023. ApJ 946(2):93

Sadaula DR, Kallman TR. 2024. ApJ 960(2):120

Salpeter EE. 1964. ApJ 140:796-800

Sazonov S, Gilfanov M, Medvedev P, Yao Y, Khorunzhev G, et al. 2021. MNRAS 508(3):3820–3847 Schmidt M. 1963. Nature 197(4872):1040

Secunda A, Jiang YF, Greene JE. 2024. ApJ 965(2):L29

Serafinelli R, De Rosa A, Tortosa A, Stella L, Vagnetti F, et al. 2024. arXiv e-prints :arXiv:2407.06769

Shakura NI, Sunyaev RA. 1973. A&A 500:33-51

Shu XW, Yaqoob T, Wang JX. 2010. ApJS 187(2):581-606

Silk J, Rees MJ. 1998. A&A 331:L1-L4

Singh KP, Garmire GP, Nousek J. 1985. ApJ 297:633-638

Sironi L, Beloborodov AM. 2020. ApJ 899(1):52

Sironi L, Spitkovsky A. 2014. ApJ 783(1):L21

Smith HJ, Hoffleit D. 1963. Nature 198(4881):650-651

Smith KL, Mushotzky RF, Boyd PT, Malkan M, Howell SB, Gelino DM. 2018. ApJ 857(2):141

Smith KL, Mushotzky RF, Koss M, Trakhtenbrot B, Ricci C, et al. 2020. MNRAS 492(3):4216–4234

Sniegowska M, Czerny B, Bon E, Bon N. 2020. A&A 641:A167

Somalwar JJ, Ravi V, Yao Y, Guolo M, Graham M, et al. 2023. arXiv e-prints :arXiv:2310.03782

Spitkovsky A. 2005. Simulations of relativistic collisionless shocks: shock structure and particle acceleration. In Astrophysical Sources of High Energy Particles and Radiation, eds. T Bulik,

B Rudak, G Madejski, vol. 801 of American Institute of Physics Conference Series. AIP

Sridhar N, García JA, Steiner JF, Connors RMT, Grinberg V, Harrison FA. 2020. ApJ 890(1):53

Sridhar N, Sironi L, Beloborodov AM. 2021. MNRAS  $507(4){:}5625{-}5640$ 

Sridhar N, Sironi L, Beloborodov AM. 2023. MNRAS 518(1):1301–1315

Stone JM, Hawley JF, Gammie CF, Balbus SA. 1996. ApJ 463:656

Stone NC, Metzger BD. 2016. MNRAS 455(1):859–883

Tagliacozzo D, Marinucci A, Ursini F, Matt G, Bianchi S, et al. 2023. MNRAS 525(3):4735-4743

Tananbaum H, Avni Y, Branduardi G, Elvis M, Fabbiano G, et al. 1979. ApJ 234:L9–L13

Tashiro M, Maejima H, Toda K, Kelley R, Reichenthal L, et al. 2018. Concept of the X-ray Astronomy Recovery Mission. In Space Telescopes and Instrumentation 2018: Ultraviolet to Gamma Ray, eds. JWA den Herder, S Nikzad, K Nakazawa, vol. 10699 of Society of Photo-Optical Instrumentation Engineers (SPIE) Conference Series

Taylor C, Reynolds CS. 2018. ApJ 855:120

Thomsen LL, Kwan TM, Dai L, Wu SC, Roth N, Ramirez-Ruiz E. 2022. ApJ 937(2):L28

Thorne KS. 1974. ApJ 191:507-520

Tichy W, Marronetti P. 2008. Phys. Rev. D 78(8):081501

Titarchuk L, Lyubarskij Y. 1995. ApJ 450:876

Tombesi F, Cappi M, Reeves JN, Nemmen RS, Braito V, et al. 2013. MNRAS 430(2):1102-1117

Tortosa A, Bianchi S, Marinucci A, Matt G, Petrucci PO. 2018. A&A 614:A37

Trakhtenbrot B, Arcavi I, MacLeod CL, Ricci C, Kara E, et al. 2019. ApJ 883(1):94

Turner SGD, Reynolds CS. 2023. MNRAS 525(2):2287-2314

Ursini F, Marinucci A, Matt G, Bianchi S, Marin F, et al. 2023. MNRAS 519(1):50-58

Ursini F, Petrucci PO, Matt G, Bianchi S, Cappi M, et al. 2016. MNRAS 463(1):382-392

Uttley P, Cackett EM, Fabian AC, Kara E, Wilkins DR. 2014. A&A Rev. 22:72

Uttley P, Malzac J. 2023. arXiv e-prints :arXiv:2312.08302

Uttley P, McHardy IM, Vaughan S. 2005. MNRAS 359(1):345-362

van Velzen S, Stone NC, Metzger BD, Gezari S, Brown TM, Fruchter AS. 2019. ApJ 878(2):82

Vasudevan RV, Fabian AC. 2007. MNRAS 381(3):1235-1251

Vasudevan RV, Mushotzky RF, Reynolds CS, Fabian AC, Lohfink AM, et al. 2014. ApJ 785:30

Vaughan S, Edelson R, Warwick RS, Uttley P. 2003. MNRAS 345(4):1271-1284

Vaughan S, Uttley P, Markowitz AG, Huppenkothen D, Middleton MJ, et al. 2016. MNRAS 461(3):3145–3152

Veledina A, Poutanen J. 2022. Polarization of Comptonized emission in slab geometry

Volonteri M, Rees MJ. 2005. Ap<br/>J633:624-629

Waddell SGH, Nandra K, Buchner J, Wu Q, Shen Y, et al. 2023. arXiv e-prints :arXiv:2306.00961

Walton DJ, Nardini E, Fabian AC, Gallo LC, Reis RC. 2013. MNRAS 428:2901–2920

Walton DJ, Nardini E, Gallo LC, Reynolds MT, Ricci C, et al. 2019. MNRAS 484:2544-2555

Walton DJ, Reis RC, Cackett EM, Fabian AC, Miller JM. 2012. MNRAS 422:2510–2531

Wang J, Kara E, García JA, Altamirano D, Belloni T, et al. 2024a. ApJ 963(1):14

Wang JM, Bon E. 2020. A&A 643:L9

Wang S, Woo JH, Gallo E, Guo H, Son D, et al. 2024b. ApJ 966(1):128

Wang Y, Ji L, García JA, Dauser T, Méndez M, et al. 2021. ApJ 906(1):11

Weisskopf MC, Soffitta P, Baldini L, Ramsey BD, O'Dell SL, et al. 2022. Journal of Astronomical Telescopes, Instruments, and Systems 8(2):026002

Wevers T, Coughlin ER, Pasham DR, Guolo M, Sun Y, et al. 2023. ApJ 942(2):L33

Wevers T, French KD, Zabludoff AI, Fischer TC, Rowlands K, et al. 2024. ApJ 970(1):L23

Wevers T, Pasham DR, Jalan P, Rakshit S, Arcodia R. 2022. A&A 659:L2

Wevers T, Pasham DR, van Velzen S, Miller-Jones JCA, Uttley P, et al. 2021. ApJ 912(2):151

Wilkins DR, Cackett EM, Fabian AC, Reynolds CS. 2016. MNRAS 458(1):200-225

Wilkins DR, Fabian AC. 2012. MNRAS 424:1284-1296

Wilkins DR, Gallo LC, Grupe D, Bonson K, Komossa S, Fabian AC. 2015. MNRAS 454(4):4440–4451

Wilkins DR, García JA, Dauser T, Fabian AC. 2020. MNRAS 498(3):3302–3319

Winkler P. F. J, White AE. 1975. ApJ 199:L139–L142

XRISM Collaboration. 2024.  $arXiv\ e\text{-}prints$ : arXiv:2408.14300

Yao PZ, Secunda A, Jiang YF, Greene JE, Villar A. 2023. ApJ 953(1):43

Yao Y, Lu W, Guolo M, Pasham DR, Gezari S, et al. 2022. ApJ 937(1):8

Yaqoob T, George IM, Nandra K, Turner TJ, Serlemitsos PJ, Mushotzky RF. 2001. ApJ 546(2):759–768

Yuan F, Narayan R. 2014. ARA&A 52:529-588

Yue M, Eilers AC, Ananna TT, Panagiotou C, Kara E, Miyaji T. 2024. arXiv e-prints :arXiv:2404.13290

Zdziarski AA, Lightman AP, Maciolek-Niedzwiecki A. 1993. ApJ 414:L93

Zeltyn G, Trakhtenbrot B, Eracleous M, Yang Q, Green P, et al. 2024. ApJ 966(1):85

Zhang W, Dovčiak M, Bursa M. 2019. ApJ 875(2):148

Zoghbi A, Fabian AC, Reynolds CS, Cackett EM. 2012. MNRAS 422:129-134

Zoghbi A, Fabian AC, Uttley P, Miniutti G, Gallo LC, et al. 2010. MNRAS 401(4):2419-2432

Zoghbi A, Miller JM, Cackett E. 2019. ApJ 884(1):26

### **APPENDIX**

Extensive time-dependent photoionization calculations that include a great amount of microphysics (e.g.; elements other than hydrogen) have been presented by Rogantini et al. (2022), Sadaula et al. (2023), Luminari et al. (2023) and Sadaula & Kallman (2024), with direct applications to astrophysical problems. Extending the discussion presented in Section 2.3, the relevant timescales for the interaction of radiation with matter in a photoionized gas are:

• Photoionization time (PI),

$$t_{\rm PI} \sim {1 \over \gamma}$$
 36.

where  $\gamma$  is the integrated radiation field F(E) weighted by the photoabsorption cross section  $\sigma(E)_i$  of a given ion i:

$$\gamma \simeq \int_{E_{\rm th}}^{1 {
m MeV}} F(E) \sigma_i(E) dE/E.$$
 37.

From here it is clear that  $t_{\rm PI}$  is mostly a function of the strength and overall shape of the local radiation field. The hydrogen photo-electric cross section can be approximated as  $\sigma(E) = (E/E_{\rm th})^3 \sigma(E_{\rm th})$ , for energies above the ionization threshold  $E_{\rm th} = 13.6\,{\rm eV}$ , or zero otherwise; and  $\sigma(E_{\rm th}) = 6.923 \times 10^{-18}\,{\rm cm}^2$ . In the case of disks illuminated by a X-ray corona, the radiation field can be approximated as power-law in energy  $F(E) = F_0 E^{-\alpha}$ , and for typical Seyfert AGN  $\alpha = 1$  (note that  $\Gamma = \alpha + 1$ , is the photon index, which is conventionally used by the X-ray community). One can then write a simple analytic approximation in the form:

$$t_{\rm PI} \sim \frac{4E_{\rm th} \ln{(1{\rm MeV}/E_{\rm th})}}{\sigma(E_{\rm th})F_0} \simeq 1.4 \times 10^8/F_{\rm x},$$
 38.

where  $F_{\rm x}$  is the net illuminating energy flux,  $F_{\rm x}=\int F(E)dE$ , which can be estimated as  $F_{\rm x}=L_{\rm x}/4\pi R^2$ . For typical AGN accreting at 10% Eddington ( $\lambda_{\rm Edd}$ ), and assuming a bolometric correction of  $\kappa_{\rm x}=0.1$  (see Section 3.1.1), the illuminating flux at the disk surface ranges  $F_{\rm x}\sim 10^{15}-10^{23}\,{\rm erg\,cm^{-2}\,s^{-1}}$ , and thus the PI times are always very short;  $t_{\rm PI}\sim 10^{-15}-10^{-7}\,{\rm s}$ . These estimates will change for a plasma containing heavier atoms that can have a larger PI cross section, but are roughly consistent with the estimates reported by Sadaula et al. (2023) (see their Fig. 1).

• Recombination time,

$$t_{\rm rec} \sim \frac{1}{n\alpha_r(T)}$$
 39.

where n is the gas density, and  $\alpha_r(T)$  is the recombination rate, which is a rather complicated function of the temperature. Recombination rates are specific to a particular state in each ion, but generally they decrease with increasing temperature, making the recombination time larger for a given density. For the hydrogen recombination rate one can adopt the fitting formula from Badnell (2006),

$$\alpha_r(T) = 8.32 \times 10^{-11} \left[ \sqrt{T/2.97} (1 + \sqrt{T/2.97})^{1-0.75} \times (1 - \sqrt{T/7 \times 10^5})^{1+0.75} \right]^{-1}.$$
40.

This equation captures the complexity of the recombination rate in the  $\sim 10^4 - 10^6 \, \mathrm{K}$  temperature range. At  $T \gtrsim 10^6 \, \mathrm{K}$  it can be approximated as  $\alpha_r(T) \approx 10^{-4} T^{-1.7}$ . A more general expression for  $t_{\rm rec}$  that includes ions other than hydrogen is given by Nicastro et al. (1999).